

Gaia Data Release 3

Exploring and mapping the diffuse interstellar band at 862 nm

Schultheis, M. ; Zhao, H. ; Zwitter, T. ; Hladczuk, N.A.; Guerra, R. ; Lammers, U. L. ; Bakker, J. ; Teodoro, P. de ; García-Lario, P. ; More Authors

DOI

[10.1051/0004-6361/202243283](https://doi.org/10.1051/0004-6361/202243283)

Publication date

2023

Document Version

Final published version

Published in

Astronomy & Astrophysics

Citation (APA)

Schultheis, M., Zhao, H., Zwitter, T., Hladczuk, N. A., Guerra, R., Lammers, U. L., Bakker, J., Teodoro, P. D., García-Lario, P., & More Authors (2023). Gaia Data Release 3: Exploring and mapping the diffuse interstellar band at 862 nm. *Astronomy & Astrophysics*, 674, Article A40. <https://doi.org/10.1051/0004-6361/202243283>

Important note

To cite this publication, please use the final published version (if applicable). Please check the document version above.

Copyright

Other than for strictly personal use, it is not permitted to download, forward or distribute the text or part of it, without the consent of the author(s) and/or copyright holder(s), unless the work is under an open content license such as Creative Commons.

Takedown policy

Please contact us and provide details if you believe this document breaches copyrights. We will remove access to the work immediately and investigate your claim.

Gaia Data Release 3

Exploring and mapping the diffuse interstellar band at 862 nm

Gaia Collaboration: M. Schultheis^{1,*}, H. Zhao¹, T. Zwitter², D. J. Marshall³, R. Drimmel⁴, Y. Frémat⁵, C. A. L. Bailer-Jones⁶, A. Recio-Blanco¹, G. Kordopatis¹, P. de Laverny¹, R. Andrae⁶, T. E. Dharmawardena⁶, M. Fouesneau⁶, R. Sordo⁷, A. G. A. Brown⁸, A. Vallenari⁷, T. Prusti⁹, J. H. J. de Bruijne⁹, F. Arenou¹⁰, C. Babusiaux^{11,10}, M. Biermann¹², O. L. Creevey¹, C. Ducourant¹³, D. W. Evans¹⁴, L. Eyer¹⁵, R. Guerra¹⁶, A. Hutton¹⁷, C. Jordi¹⁸, S. A. Klioner¹⁹, U. L. Lammers¹⁶, L. Lindegren²⁰, X. Luri¹⁸, F. Mignard¹, C. Panem²¹, D. Pourbaix^{22,23,†}, S. Randich²⁴, P. Sartoretti¹⁰, C. Soubiran¹³, P. Tanga¹, N. A. Walton¹⁴, U. Bastian¹², F. Jansen^{25,★}, D. Katz¹⁰, M. G. Lattanzi^{4,26}, F. van Leeuwen¹⁴, J. Bakker¹⁶, C. Cacciari²⁷, J. Castañeda²⁸, F. De Angeli¹⁴, C. Fabricius¹⁸, L. Galluccio¹, A. Guerrier²¹, U. Heiter²⁹, E. Masana¹⁸, R. Messineo³⁰, N. Mowlavi¹⁵, C. Nicolas²¹, K. Nienartowicz^{31,32}, F. Pailler²¹, P. Panuzzo¹⁰, F. Riclet²¹, W. Roux²¹, G. M. Seabroke³³, F. Thévenin¹, G. Gracia-Abril^{34,12}, J. Portell¹⁸, D. Teyssier³⁵, M. Altmann^{12,36}, M. Audard^{15,32}, I. Bellas-Velidis³⁷, K. Benson³³, J. Berthier³⁸, R. Blomme⁵, P. W. Burgess¹⁴, D. Busonero⁴, G. Busso¹⁴, H. Cánovas³⁵, B. Carry¹, A. Cellino⁴, N. Cheek³⁹, G. Clementini²⁷, Y. Damerdjij^{40,41}, M. Davidson⁴², P. de Teodoro¹⁶, M. Nuñez Campos¹⁷, L. Delchambre⁴⁰, A. Dell’Oro²⁴, P. Esquej⁴³, J. Fernández-Hernández⁴⁴, E. Fraile⁴³, D. Garabato⁴⁵, P. García-Lario¹⁶, E. Gosset^{40,23}, R. Haigron¹⁰, J.-L. Halbwachs⁴⁶, N. C. Hambly⁴², D. L. Harrison^{14,47}, J. Hernández¹⁶, D. Hestroffer³⁸, S. T. Hodgkin¹⁴, B. Holl^{15,32}, K. Janßen⁴⁸, G. Jevardat de Fombelle¹⁵, S. Jordan¹², A. Krone-Martins^{49,50}, A. C. Lanzafame^{51,52}, W. Löffler¹², O. Marchal⁴⁶, P. M. Marrese^{53,54}, A. Moitinho⁴⁹, K. Muinonen^{55,56}, P. Osborne¹⁴, E. Pancino^{24,54}, T. Pauwels⁵, C. Reylé⁵⁷, M. Riello¹⁴, L. Rimoldini³², T. Roegiers⁵⁸, J. Rybizki⁶, L. M. Sarro⁵⁹, C. Siopis²², M. Smith³³, A. Sozzetti⁴, E. Utrilla¹⁷, M. van Leeuwen¹⁴, U. Abbas⁴, P. Abraham^{60,61}, A. Abreu Aramburu⁴⁴, C. Aerts^{62,63,6}, J. J. Aguado⁵⁹, M. Ajaj¹⁰, F. Aldea-Montero¹⁶, G. Altavilla^{53,54}, M. A. Álvarez⁴⁵, J. Alves⁶⁴, F. Anders¹⁸, R. I. Anderson⁶⁵, E. Anglada Varela⁴⁴, T. Antoja¹⁸, D. Baines³⁵, S. G. Baker³³, L. Balaguer-Núñez¹⁸, E. Balbinot⁶⁶, Z. Balog^{12,6}, C. Barache³⁶, D. Barbato^{15,4}, M. Barros⁴⁹, M. A. Barstow⁶⁷, S. Bartolomé¹⁸, J.-L. Bassilana⁶⁸, N. Bauchet¹⁰, U. Becciani⁵¹, M. Bellazzini²⁷, A. Berihuete⁶⁹, M. Bernet¹⁸, S. Bertone^{70,71,4}, L. Bianchi⁷², A. Binnenfeld⁷³, S. Blanco-Cuaresma⁷⁴, T. Boch⁴⁶, A. Bombrun⁷⁵, D. Bossini⁷⁶, S. Bouquillon^{36,77}, A. Bragaglia²⁷, L. Bramante³⁰, E. Breedt¹⁴, A. Bressan⁷⁸, N. Brouillet¹³, E. Brugaletta⁵¹, B. Bucciarelli^{4,26}, A. Burlacu⁷⁹, A. G. Butkevich⁴, R. Buzzì⁴, E. Caffau¹⁰, R. Cancelliere⁸⁰, T. Cantat-Gaudin^{18,6}, R. Carballo⁸¹, T. Carlucci³⁶, M. I. Carnerero⁴, J. M. Carrasco¹⁸, L. Casamiquela^{13,10}, M. Castellani⁵³, A. Castro-Ginard⁸, L. Chaoul²¹, P. Charlot¹³, L. Chemin⁸², V. Chiaramida³⁰, A. Chiavassa¹, N. Chornay¹⁴, G. Comoretto^{35,83}, G. Contursi¹, W. J. Cooper^{84,4}, T. Cornez⁶⁸, S. Cowell¹⁴, F. Crifo¹⁰, M. Cropper³³, M. Crosta^{4,85}, C. Crowley⁷⁵, C. Dafonte⁴⁵, A. Dapergolas³⁷, P. David³⁸, F. De Luise⁸⁶, R. De March³⁰, J. De Ridder⁶², R. de Souza⁸⁷, A. de Torres⁷⁵, E. F. del Peloso¹², E. del Pozo¹⁷, M. Delbo¹, A. Delgado⁴³, J.-B. Delisle¹⁵, C. Demouchy⁸⁸, S. Diakite⁸⁹, C. Diener¹⁴, E. Distefano⁵¹, C. Dolding³³, H. Enke⁴⁸, C. Fabre⁹⁰, M. Fabrizio^{53,54}, S. Faigler⁹¹, G. Fedorets^{55,92}, P. Fernique^{46,93}, F. Figueras¹⁸, Y. Fournier⁴⁸, C. Fouron⁷⁹, F. Fragkoudi^{94,95,96}, M. Gai⁴, A. Garcia-Gutierrez¹⁸, M. Garcia-Reinaldos¹⁶, M. García-Torres⁹⁷, A. Garofalo²⁷, A. Gavel²⁹, P. Gavras⁴³, E. Gerlach¹⁹, R. Geyer¹⁹, P. Giacobbe⁴, G. Gilmore¹⁴, S. Girona⁹⁸, G. Giuffrida⁵³, R. Gomel⁹¹, A. Gomez⁴⁵, J. González-Núñez^{39,99}, I. González-Santamaría⁴⁵, J. J. González-Vidal¹⁸, M. Granvik^{55,100}, P. Guillout⁴⁶, J. Guiraud²¹, R. Gutiérrez-Sánchez³⁵, L. P. Guy^{32,101}, D. Hatzidimitriou^{102,37}, M. Hauser^{6,103}, M. Haywood¹⁰, A. Helmer⁶⁸, A. Helmi⁶⁶, M. H. Sarmiento¹⁷, S. L. Hidalgo^{104,105}, N. Hładczuk^{16,106}, D. Hobbs²⁰, G. Holland¹⁴, H. E. Huckle³³, K. Jardine¹⁰⁷, G. Jasniewicz¹⁰⁸, A. Jean-Antoine Piccolo²¹, Ó. Jiménez-Arranz¹⁸, J. Juaristi Campillo¹², F. Julbe¹⁸, L. Karbevská^{32,109}, P. Kervella¹¹⁰, S. Khanna^{66,4}, A. J. Korn²⁹, Á. Kóspál^{160,6,61}, Z. Kostrzewa-Rutkowska^{8,111}, K. Kruszyńska¹¹², M. Kun⁶⁰, P. Laizeau¹¹³, S. Lambert³⁶, A. F. Lanza⁵¹, Y. Lasne⁶⁸, J.-F. Le Campion¹³,

* Corresponding author: M. Schultheis, e-mail: mathias.schultheis@oca.eu

** Retired.

Y. Lebreton^{110,114}, T. Lebzelter⁶⁴, S. Leccia¹¹⁵, N. Leclerc¹⁰, I. Lecoœur-Taibi³², S. Liao^{116,4,117}, E. L. Licata⁴, H. E. P. Lindström^{4,118,119}, T. A. Lister¹²⁰, E. Livanou¹⁰², A. Lobel⁵, A. Lorca¹⁷, C. Loup⁴⁶, P. Madrero Pardo¹⁸, A. Magdaleno Romeo⁷⁹, S. Managau⁶⁸, R. G. Mann⁴², M. Manteiga¹²¹, J. M. Marchant¹²², M. Marconi¹¹⁵, J. Marcos³⁵, M. M. S. Marcos Santos³⁹, D. Marín Pina¹⁸, S. Marinoni^{53,54}, F. Marocco¹²³, L. Martin Polo³⁹, J. M. Martín-Fleitas¹⁷, G. Marton⁶⁰, N. Mary⁶⁸, A. Masip¹⁸, D. Massari²⁷, A. Mastrobuono-Battisti¹⁰, T. Mazeh⁹¹, P. J. McMillan²⁰, S. Messina⁵¹, D. Michalik⁹, N. R. Millar¹⁴, A. Mints⁴⁸, D. Molina¹⁸, R. Molinaro¹¹⁵, L. Molnár^{60,124,61}, G. Monari⁴⁶, M. Monguió¹⁸, P. Montegriffo²⁷, A. Montero¹⁷, R. Mor¹⁸, A. Mora¹⁷, R. Morbidelli⁴, T. Morel⁴⁰, D. Morris⁴², T. Muraveva²⁷, C. P. Murphy¹⁶, I. Musella¹¹⁵, Z. Nagy⁶⁰, L. Noval⁶⁸, F. Ocaña^{35,125}, A. Ogden¹⁴, C. Ordenovic¹, J. O. Osinde⁴³, C. Pagani⁶⁷, I. Pagano⁵¹, L. Palaversa^{126,14}, P. A. Palicio¹, L. Pallas-Quintela⁴⁵, A. Panahi⁹¹, S. Payne-Wardenaar¹², X. Peñalosa Esteller¹⁸, A. Penttilä⁵⁵, B. Pichon¹, A. M. Piersimoni⁸⁶, F.-X. Pineau⁴⁶, E. Plachy^{60,124,61}, G. Plum¹⁰, E. Poggio^{1,4}, A. Prša¹²⁷, L. Pulone⁵³, E. Racero^{39,125}, S. Ragaini²⁷, M. Rainer^{24,128}, C. M. Raiteri⁴, P. Ramos^{18,46}, M. Ramos-Lerate³⁵, P. Re Fiorentin⁴, S. Regibo⁶², P. J. Richards¹²⁹, C. Rios Diaz⁴³, V. Ripepi¹¹⁵, A. Riva⁴, H.-W. Rix⁶, G. Rixon¹⁴, N. Robichon¹⁰, A. C. Robin⁵⁷, C. Robin⁶⁸, M. Roelens¹⁵, H. R. O. Rogues⁸⁸, L. Rohrbasser³², M. Romero-Gómez¹⁸, N. Rowell⁴², F. Royer¹⁰, D. Ruz Mieres¹⁴, K. A. Rybicki¹¹², G. Sadowski²², A. Sáez Núñez¹⁸, A. Sagristà Sellés¹², J. Sahlmann⁴³, E. Salguero⁴⁴, N. Samaras^{5,130}, V. Sanchez Gimenez¹⁸, N. Sanna²⁴, R. Santoveña⁴⁵, M. Sarasso⁴, E. Sciacca⁵¹, M. Segol⁸⁸, J. C. Segovia³⁹, D. Ségransan¹⁵, D. Semeux⁹⁰, S. Shahaf¹³¹, H. I. Siddiqui¹³², A. Siebert^{46,93}, L. Siltala⁵⁵, A. Silvelo⁴⁵, E. Slezak¹, I. Slezak¹, R. L. Smart⁴, O. N. Snaith¹⁰, E. Solano¹³³, F. Solitro³⁰, D. Souami^{110,134}, J. Souchay³⁶, A. Spagna⁴, L. Spina⁷, F. Spoto⁷⁴, I. A. Steele¹²², H. Steidelmüller¹⁹, C. A. Stephenson^{35,135}, M. Süveges¹³⁶, J. Surdej^{40,137}, L. Szabados⁶⁰, E. Szegedi-Elek⁶⁰, F. Taris³⁶, M. B. Taylor¹³⁸, R. Teixeira⁸⁷, L. Tolomei³⁰, N. Tonello⁹⁸, F. Torra²⁸, J. Torra^{18,†}, G. Torralba Elipe⁴⁵, M. Trabucchi^{139,15}, A. T. Tsounis¹⁴⁰, C. Turon¹⁰, A. Ulla¹⁴¹, N. Unger¹⁵, M. V. Vaillant⁶⁸, E. van Dillen⁸⁸, W. van Reeve¹⁴², O. Vanel¹⁰, A. Vecchiato⁴, Y. Viala¹⁰, D. Vicente⁹⁸, S. Voutsinas⁴², M. Weiler¹⁸, T. Wevers^{14,143}, Ł. Wyrzykowski¹¹², A. Yoldas¹⁴, P. Yvard⁸⁸, J. Zorec¹⁴⁴, and S. Zucker⁷³

(Affiliations can be found after the references)

Received 8 February 2022 / Accepted 19 April 2022

ABSTRACT

Context. Diffuse interstellar bands (DIBs) are common interstellar absorption features in spectroscopic observations but their origins remain unclear. DIBs play an important role in the life cycle of the interstellar medium (ISM) and can also be used to trace Galactic structure.

Aims. Here, we demonstrate the capacity of the *Gaia*-Radial Velocity Spectrometer (RVS) in *Gaia* DR3 to reveal the spatial distribution of the unknown molecular species responsible for the most prominent DIB at 862 nm in the RVS passband, exploring the Galactic ISM within a few kiloparsecs from the Sun.

Methods. The DIBs are measured within the GSP-Spec module using a Gaussian profile fit for cool stars and a Gaussian process for hot stars. In addition to the equivalent widths and their uncertainties, *Gaia* DR3 provides their characteristic central wavelength, width, and quality flags.

Results. We present an extensive sample of 476 117 individual DIB measurements obtained in a homogeneous way covering the entire sky. We compare spatial distributions of the DIB carrier with interstellar reddening and find evidence that DIB carriers are present in a local bubble around the Sun which contains nearly no dust. We characterised the DIB equivalent width with a local density of $0.19 \pm 0.04 \text{ \AA kpc}^{-1}$ and a scale height of $98.60_{-8.46}^{+11.10}$ pc. The latter is smaller than the dust scale height, indicating that DIBs are more concentrated towards the Galactic plane. We determine the rest-frame wavelength with unprecedented precision ($\lambda_0 = 8620.86 \pm 0.019 \text{ \AA}$ in air) and reveal a remarkable correspondence between the DIB velocities and the CO gas velocities, suggesting that the 862 nm DIB carrier is related to macro-molecules.

Conclusions. We demonstrate the unique capacity of *Gaia* to trace the spatial structure of the Galactic ISM using the 862 nm DIB.

Key words. ISM: lines and bands – ISM: kinematics and dynamics – dust, extinction

1. Introduction

Diffuse interstellar bands (DIBs) are interstellar absorption features that primarily exist in the optical and near-infrared (NIR) wavelength range, the physical origin of which is still debated. The name was formally given by Merrill (1930), where ‘diffuse’ refers to the fact that their profiles are broader than those of interstellar atomic lines (e.g., NaI lines). DIBs presumably originate from molecular absorption, which is supported by the fact that

their central wavelength does not match any known atomic transition lines. The fine structure observed in some DIBs also suggests that the molecular carriers are probably in the gas phase. For reviews on DIBs, see Leger & Puget (1984), Herbig (1995), Sarre (2006), and Snow & McCall (2006).

Nowadays, molecules are strongly suggested to be associated with the DIB carrier, because DIB profiles are usually much broader than atomic lines and contain substructures even through single-cloud sight lines (e.g., Sarre et al. 1995, Cami et al. 1997, Kerr et al. 1998, Galazutdinov et al. 2008). Carbon-bearing molecules are the most favoured species in this

† Deceased.

respect as carbon can form many stable compounds and is relatively abundant in the Universe (Puget & Leger 1989)

The DIB at 862 nm (hereafter referred to as DIB $\lambda 862$) is a strong band, but was not identified until 1975 (Geary 1975), more than 50 yr after the discovery of the first DIBs, because the wavelength range beyond 8600 Å was not covered by earlier work. The DIB $\lambda 862$ was confirmed by Sanner et al. (1978), who further reported $\lambda_0 = 8620.7 \pm 0.3$ Å and a tight linear correlation between the DIB equivalent width (EW_{862}) and the colour excess, that is $E(B - V) = 2.85 \pm 0.11 \times EW_{862}$ (coefficient calculated by Kos et al. 2013). Munari (1999, 2000) made preliminary studies of the relation between the EW_{862} of DIB $\lambda 862$ and interstellar extinction. This author found a surprisingly tight correlation with $E(B - V)/EW_{862} = 2.63$ (Munari 1999) and 2.69 ± 0.03 (Munari 2000), respectively. Therefore, the DIB $\lambda 862$ was suggested to be a tracer of Galactic extinction in the context of the *Gaia* mission, while Krelowski (2018) and Krelowski et al. (2019) argued that $E(B - V)/EW_{862}$ can vary depending on the line of sight. Munari et al. (2008) measured the DIB $\lambda 862$ in the spectra of 68 early-type stars observed by the Radial Velocity Experiment (RAVE; Steinmetz et al. 2006) and derived a very good correlation between EW_{862} and $E(B - V)$ with $E(B - V)/EW_{862} = 2.72 \pm 0.03$. These results, as well as those of Munari (1999, 2000), were all consistent with each other, but none agreed with those of Wallerstein et al. (2007), who derived a much higher ratio of $E(B - V)/EW_{862}$.

Munari et al. (2008) determined the rest-frame wavelength of DIB $\lambda 862$ as $\lambda_0 = 8620.4 \pm 0.1$ Å based on the assumption that the average velocity of their carriers towards the Galactic center is approximately zero, as derived from the interstellar-medium (ISM) radial-velocity map of Brand & Blitz (1993).

To make use of the vast number of cool-star ($3500 \leq T_{\text{eff}} \leq 7000$ K) spectra in RAVE, Kos et al. (2013) implemented a data-driven method to derive the EW_{862} of interstellar spectra using real spectra at high Galactic latitudes ($b < -65^\circ$) and furthermore stacked spectra in small spatial volumes to increase the final signal-to-noise ratio (S/N) and measure EW_{862} with high precision. In this way, they confirmed the linear $EW_{862} - E(B - V)$ correlation in a statistical way.

Based on measurements with a large number of RAVE spectra, Kos et al. (2014) built the first projected DIB $\lambda 862$ intensity map, mainly within 3 kpc from the Sun, where for the first time the large-scale structure of the distribution of the DIB $\lambda 862$ carrier was shown. The findings of these authors further suggested an exponential distribution of EW_{862} in the direction perpendicular to the Galactic plane with a scale height of 209.0 ± 11.9 pc, larger than the scale height of 117.7 ± 4.7 pc for the dust derived by their A_V map. Puspitarini et al. (2015) measured the DIB $\lambda 862$ in the spectra of 64 late-type stars from the *Gaia*-ESO (GES) survey (Gilmore et al. 2012) towards a Galactic anticentre region at $(l, b) = (212.9^\circ, -2.0^\circ)$. Puspitarini et al. (2015) fitted the observed spectra with synthetic spectra containing stellar components, telluric transmissions, and a DIB empirical profile. For DIB $\lambda 862$, they obtained the empirical model by averaging the profiles detected in several spectra based on the data analysis reported by Chen et al. (2013).

Similar to Puspitarini et al. (2015), Krelowski et al. (2019) also argued that a simple Gaussian fit was not enough to describe the irregular profile of the DIB $\lambda 862$. They therefore used the observation towards BD + 40 4220, a heavily reddened and rapidly rotating star, as a template for the profile of $\lambda 862$. Measurements of other targets were obtained by rescaling the depth of the template to match the observed band profiles.

Using this method, Krelowski et al. (2019) measured 56 high-resolution spectra ($R > 30000$) and derived a ratio

of $E(B - V)/EW_{862} = 2.03 \pm 0.15$ with an offset of 0.22, which was close to the result of Puspitarini et al. (2015). Maíz Apellániz (2015) showed a linear relation between EW_{862} and the colour excess $E(4405 - 5495)$ up to $A_V \sim 6$ mag with a Pearson coefficient of $r_p = 0.878$. All previous studies suggested a linear relation between EW_{862} and extinction except Damineli et al. (2016), who reported a quadratic relation based on the observations of 12 bright field stars and 11 members of Westerlund 1 cluster. Their relation is in good agreement with those found by Wallerstein et al. (2007) and Munari et al. (2008) for $EW_{862} < 0.8$ Å.

In this paper, we discuss the DIB $\lambda 862$ measurements of nearly half a million DIBs measured by the RVS spectrometer. This is, by one order of magnitude, the largest sample of individual DIB measurements with full sky-coverage to be obtained so far.

In Sect. 2, we discuss the DIB $\lambda 862$ sample. In Sect. 3 we define our high-quality sample and in Sect. 4 we validate the DIB $\lambda 862$ measurements in the HR diagram. In Sect. 5 we show the correlation with the dust extinction and in Sect. 6 we present our analysis of the spatial distribution of the DIBs $\lambda 862$. In Sect. 7 we describe how we determined the rest-frame wavelength of DIB $\lambda 862$, and in Sect. 8 we look briefly at an application to kinematic studies. We conclude in Sect. 9.

2. Description of the sample of diffuse interstellar bands

This work makes use of the DIB $\lambda 862$ parameterisation derived from the *Gaia* RVS spectra using the General Stellar Parameteriser spectroscopy (GSP-Spec, Recio-Blanco et al. 2023) module and made available through the astrophysical_parameters table of the *Gaia* third data release (DR3). We note that the RVS wavelength range is [845, 870] nm (Sartoretti et al. 2018), and its medium resolving power is $R = \lambda/\Delta\lambda \sim 11500$ (Cropper et al. 2018). In addition to the DIB $\lambda 862$ parameterisation, GSP-Spec estimates the main atmospheric parameters and the individual abundances of 12 different chemical elements from *Gaia* RVS spectra of single stars. When necessary (e.g., stars with $T_{\text{eff}} < 7000$ K), the DIB $\lambda 862$ spectral parameterisation is based on the MatisseGauguin GSP-Spec workflow. More details on the DIB $\lambda 862$ measurement algorithms can be found in Zhao et al. (2021a). A GSP-Spec catalogue flag was implemented (Recio-Blanco et al. 2023) during the post-processing with a chain of 41 digits including all the adopted failure criteria and uncertainty sources considered during the post-processing. In this chain, value ‘0’ is the best, and ‘9’ is the worst, generally implying the parameter masking. For our purposes, we use only the first 13 characters (see Sect. 3, Table 1).

We performed a local renormalisation of the spectrum around the DIB $\lambda 862$ feature (35 Å wide around its central wavelength) for each *Gaia*-RVS spectrum. We carried out a preliminary fit using a preliminary detection of the DIB $\lambda 862$ profile and sources where noise is at the level of or exceeds the depth of the DIB $\lambda 862$ feature were eliminated. Only detections above the 3σ -level are considered as true detections. In order to perform the main fitting process of the DIB $\lambda 862$, our sample is separated into cool ($3500 < T_{\text{eff}} \leq 7000$ K) and hot ($T_{\text{eff}} > 7000$ K) stars. For cool stars, we divided the observed spectrum by the best matching synthetic spectrum from GSP-Spec (corresponding to the derived atmospheric parameters), and fitted the DIB $\lambda 862$ profile with a Gaussian function and a constant that accounts for the continuum:

$$f_{\odot}(\lambda; p_0, p_1, p_2) = p_0 \times \exp\left(-\frac{(\lambda - p_1)^2}{2p_2^2}\right) + C, \quad (1)$$

Table 1. Definition of our high-quality sample.

QF	≤ 2
$\text{err}(\text{EW}_{862})/\text{EW}_{862}$	≤ 0.35
C_{obs}	8620–8626 Å
GSP-Specflag(vbroadT)	≤ 1
GSP-Specflag(vbroadG)	≤ 1
GSP-Specflag(vbroadM)	≤ 1
GSP-Specflag(vradT)	≤ 1
GSP-Specflag(vradG)	≤ 1
GSP-Specflag(vradM)	≤ 1
GSP-Specflag(fluxNoise)	≤ 1
GSP-Specflag(extrapol)	≤ 1
GSP-Specflag(negFlux)	≤ 1
GSP-Specflag(nanFlux)	≤ 1
GSP-Specflag(emission)	≤ 1
GSP-Specflag(nullFluxErr)	≤ 1
GSP-Specflag(KMgiantPar)	≤ 1

where p_0 and p_2 are the depth and width of the DIB profile, p_1 is the measured central wavelength, C is the constant continuum, and λ is the spectral wavelength.

For hot stars, we applied a Gaussian process similar to Kos (2017) in which the DIB $\lambda 862$ profile is fitted by a Gaussian process regression (Gershman & Blei 2012). In order to extract the information of the DIB feature, we applied a Gaussian mean function (Eq. (1)) with $C \equiv 1$. For the kernels, we followed the strategy of Kos (2017) and used exponential-squared kernel models for the stellar absorption lines:

$$k_{\text{se}}(x, x') = a \exp\left(-\frac{\|x - x'\|^2}{2l^2}\right), \quad (2)$$

and a Matérn 3/2 kernel model for the correlated noise:

$$k_{m3/2}(x, x') = a \left(1 + \frac{\sqrt{3}\|x - x'\|}{l}\right) \exp\left(-\frac{\sqrt{3}\|x - x'\|}{l}\right), \quad (3)$$

where a scales the kernels, and l is the characteristic width of each kernel. We refer to Zhao et al. (2021a) for a more detailed description of this process.

For each of the sources, the EW_{862} , depth (p_0), central wavelength (p_1), and width (p_2) together with their uncertainties are determined with $\text{EW}_{862} = \sqrt{2\pi} \times |p_0| \times p_2/C$ where C is the continuum level and $p_2 = \text{FWHM}/(2\sqrt{2\ln(2)})$, where FWHM is the full width at half maximum of the DIB $\lambda 862$ profile.

We consider two main uncertainties on the derived EW: the random noise error (σ_{noise}), which is related to the signal-to-noise ratio (S/N) of the spectrum, and the mismatch between the observed spectrum and the synthetic one (σ_{spect}). σ_{noise} was estimated for different DIB profiles using a random-noise simulation (see Sect. 2.6 in Zhao et al. 2021a for more details). The total uncertainty of the EW is considered to be $\sigma_{\text{EW}}^2 = \sigma_{\text{noise}}^2 + \sigma_{\text{spect}}^2$. We refer to Zhao et al. (2021a) for a more detailed description of the derived uncertainties.

Quality flags (QFs) ranging from QF=0 (highest quality) to QF=5 (lowest quality) are generated. The defined values of the QF depend on the parameters p_0 , p_1 , and p_2 , but also on the global noise level R_A defined by the standard deviation of the data–model residuals between 8605 and 8640 Å as well as the local noise level R_B within the DIB $\lambda 862$ profile. Table 2 shows the definition of the QF values. For a more detailed description

Table 2. Definition of the quality flags.

QF	p_0	p_2 (Å)	N
0	$<0.15 \text{ AND } > \max(R_A, R_B)$	1.2–3.2	180 879
1	$<0.15 \text{ AND } < \max(R_A, R_B) \text{ \& } > R_B$	1.2–3.2	1149
2	$<0.15 \text{ AND } > \max(R_A, R_B)$	0.6–1.2	54 808
3	$<0.15 \text{ AND } < \max(R_A, R_B) \text{ \& } > R_B$	0.6–1.2	679
4	$<0.15 \text{ AND } < \max(R_A, R_B) \text{ \& } < R_B$	0.6–1.2	2843
5	<0.15	–	235 759

Notes. R_A is the fitting residual between the observed and synthetic spectrum for the global RVS spectrum, and R_B is the region close to the DIB $\lambda 862$ feature. Targets with a central wavelength beyond 816.6–8628.1 Å in vacuum are all labelled as QF = 5. The last column gives the number of sources for each QF.

of QF, we refer to Zhao et al. (2021a) and Recio-Blanco et al. (2023). In this paper, we concentrate on a high-quality sample (QF ≤ 2 , see Sect. 3) but we stress that the full DIB $\lambda 862$ sample should be scientifically exploited; for example, weak DIBs $\lambda 862$ in low extinction areas.

The full GSP-Spec sample contains 5 591 594 sources. Of these, 476 117 have a valid DIB $\lambda 862$ measurement ($\sim 8.5\%$). The number of sources for each QF is specified in Table 2.

Figure 1 shows the distribution on the sky of the DIB $\lambda 862$ measurements at a resolution of 1.8° (HEALPix map with level 5). As expected, the DIBs $\lambda 862$ are concentrated towards the Galactic plane which is even more pronounced for the high-quality DIBs $\lambda 862$ (right panel).

Figure 2 displays the relation between EW_{862} and the E(BP – RP) interstellar reddening measure from GSP-Phot (Andrae et al. 2023). We see that DIBs $\lambda 862$ with low QFs (QF > 2) show very small EW_{862} but a large range of E(BP – RP) which is not the case for the high quality (HQ) DIB $\lambda 862$ measurements (QF ≤ 2 , see Sect. 3).

3. Definition of the high-quality sample

Figure 3 displays the GSP-Spec Kiel diagram of a subsample with QF < 5 as a function of the fractional uncertainty of the EW_{862} . The vast majority of our sources show typical uncertainties below 20%. However, on the red giant branch (RGB) sequence, the cooler stars (which are in general metal-richer) show larger uncertainties compared to the hotter ones. This can be explained by the fact that for cooler metal-rich stars, in general, we see a poorer agreement between the observed and the synthetic spectra due to the presence of molecular bands. This is also revealed by the larger $\log \chi^2$ values from GSP-spec.

We also notice higher uncertainties for hot dwarf stars in the range $7000 < T_{\text{eff}} < 8000$ K. The majority of those stars are classified as very metal-poor with $[\text{M}/\text{H}] < -3$ dex by GSP-Spec. They further exhibit very large $v \sin i$ values from ESP-HS (Extended Stellar Parametrizer for Hot Stars; see Sect. 5.3). In addition to the parameter degeneracy between T_{eff} and $[\text{M}/\text{H}]$ for high-temperature stars, these objects present large $v \sin i$ values, which are not taken into account in the present GSP-Spec parameterisation, inducing parameter biases (cf. Recio-Blanco et al. 2023). Applying the specifically defined GSP-Spec flags (see Table 1) removes the majority of these stars.

Figure 4 shows the distribution of the fractional uncertainties ($\text{err}(\text{EW}_{862})/\text{EW}_{862}$) with QF < 5 . A clear bimodal distribution is apparent that is related to cool stars ($T_{\text{eff}} < 4500$ K) with relatively weak DIBs $\lambda 862$ (< 0.2 Å) and a mismatch between

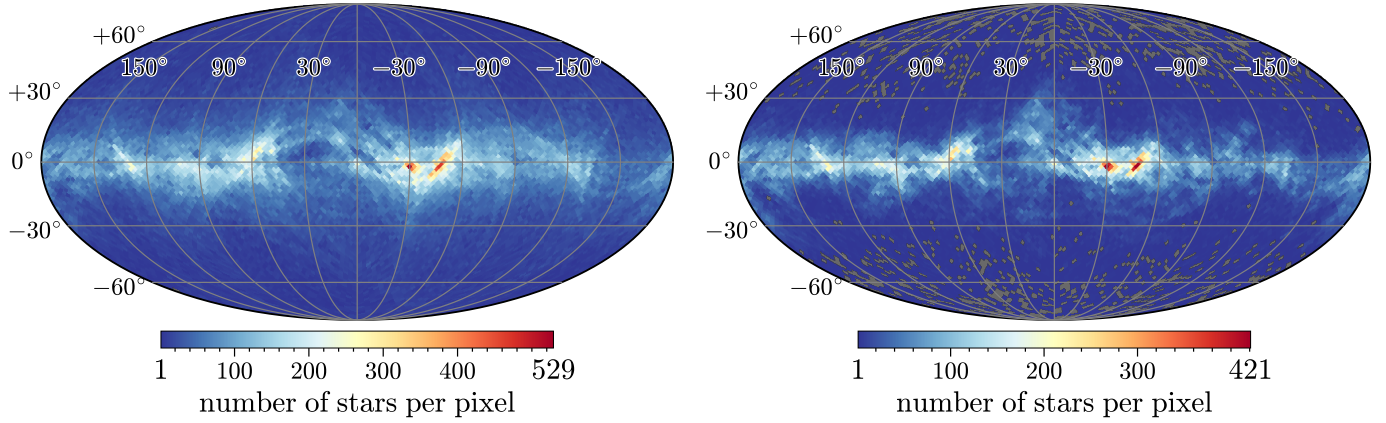


Fig. 1. *Left panel:* galactic distribution of the 476 117 DIBs $\lambda 862$ in *Gaia* DR3. The spatial resolution is 1.8° per HEALpixel (level 5). The colour scale indicates the number of measurements per pixel. *Right panel:* the subset of 236 836 sources with high-quality measurements ($QF \leq 2$, see Sect. 3).

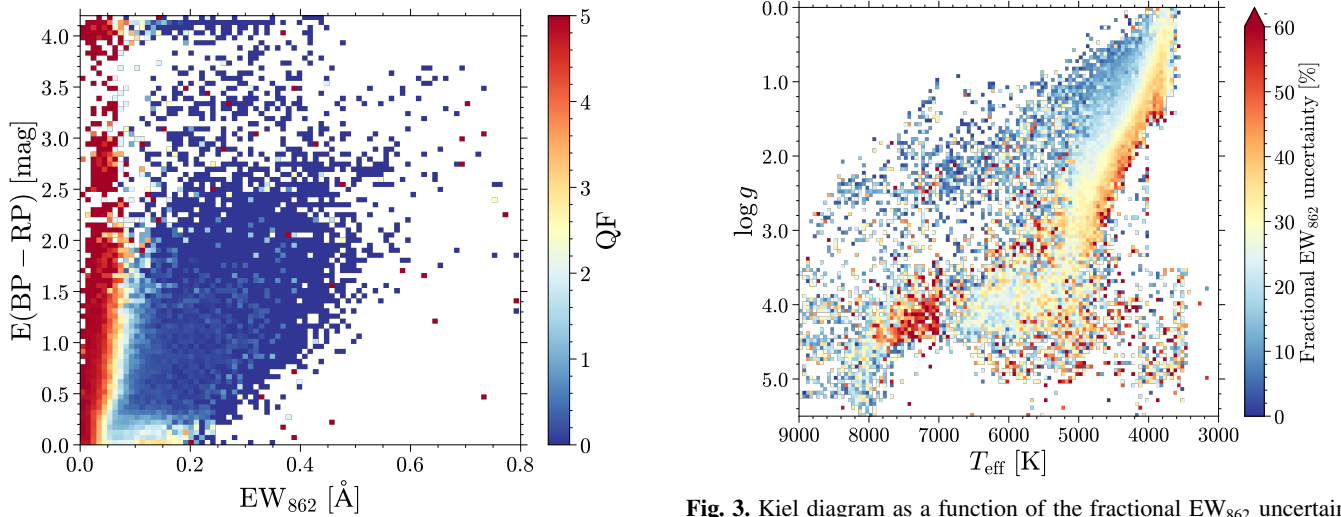


Fig. 2. Equivalent width vs. $E(BP - RP)$ for the DIB $\lambda 862$ sample coloured by the mean QF calculated in $0.01 \text{ \AA} \times 0.05 \text{ mag}$ bins.

the observed and the synthetic spectrum. We decided to reject sources with uncertainties larger than 35%. In addition, we decided to neglect DIB $\lambda 862$ measurements outside the wavelength interval $8620 < C_{\text{obs}} < 8626 \text{ \AA}$ – where C_{obs} is the measured central wavelength in the heliocentric frame with $C_{\text{obs}} = p_1 + v_{\text{rad}} \times p_1/c$ where v_{rad} is the stellar radial velocity and c the velocity of light – because the majority of those are weak DIBs $\lambda 862$, where the determination of the p_1 parameter could be corrupted and lead to high, unrealistic velocities. We stress that p_1 and C_{obs} are reported in the vacuum.

Our HQ sample is defined based on the criteria specified in Table 1 which comprises 141 103 objects. For a detailed explanation of the GSP-spec flag we refer here to Recio-Blanco et al. (2023).

4. The Kiel diagram

Figure 5 shows the Kiel diagram colour-coded as a function of the EW_{862} (left panel), the corresponding *Gaia* distances from *Gaia* EDR3 (middle panel, Bailer-Jones et al. 2021), and the DIB $\lambda 862$ width (p_2). The very similar trend in these diagrams

is striking, and indicates a clear relation between the EW_{862} of the DIB $\lambda 862$ carrier and its distance, that is stars with larger distances show larger EW_{862} . This is to be expected: as an interstellar feature, the DIB $\lambda 862$ profile measured in the spectrum of a background star is the result of an integration of the DIB $\lambda 862$ carrier between the observer and the star. DIB $\lambda 862$ strength and dust extinction increase along the line of sight, and so both of them correlate with the distance and therefore also with each other. Also, we note that the distance of the background star is only an upper limit to the true distance of the DIB $\lambda 862$ carrier clouds along the line of sight (Zasowski et al. 2015). As shown by Zhao et al. (2021b), direct measurements of the DIB $\lambda 862$ carrier clouds can be obtained using kinematic distances. This method will be further investigated in another paper.

The right panel of Fig. 5 shows how the measured width of the DIB $\lambda 862$ (the value of the parameter p_2) increases with decreasing surface gravity; that is, we see that widths in giants are generally larger than in dwarfs. One may also conclude that the widths of DIB $\lambda 862$ absorptions increase with distance, and explain this as a consequence of a superposition of an increasing number of clouds at slightly different radial velocities which accumulate along the line of sight. However, we also see

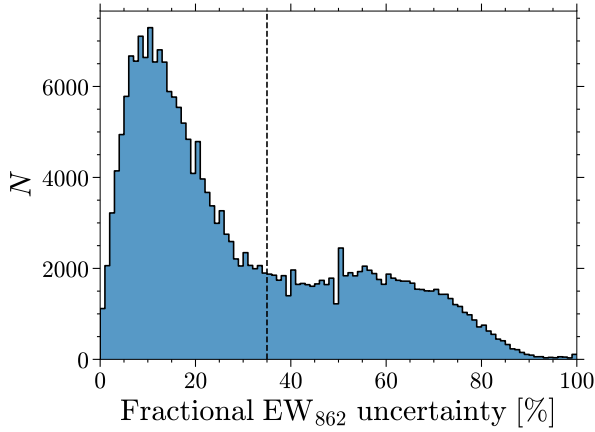


Fig. 4. Histogram of the fractional uncertainties $\text{err}(EW_{862})/EW_{862}$ for targets with $QF < 5$. The dashed line shows the cut-off in the uncertainties at 35%.

DIB $\lambda 862$ with large widths for close-by stars with $T_{\text{eff}} < 5000$ K and $\log g > 3$. This could be a consequence of spectral mismatches between observed spectra and the templates we use. These systematic trends will be investigated in a future work, but for now we stress that the measured widths of the DIB $\lambda 862$ should be interpreted with caution.

From Fig. 5 we see that stars with $5000 < T_{\text{eff}} < 7000$ K and $\log g < 2.5$ have strong DIBs $\lambda 862$. These massive stars lie at distances of between 2 and 4 kpc and most of them are located in the closest spiral arms (e.g., Sagittarius/Carina, Local and Perseus arms). This is in perfect agreement with the findings of Recio-Blanco et al. (2023), who clearly identified those objects in their GSP-Spec Kiel diagram as massive stars that are tracers of the spiral arm structure, in agreement with the spatial maps derived from Poggio et al. (2021). The DIB $\lambda 862$ measurements can therefore be considered as an excellent tracer of spiral arm structures.

In contrast, our HQ sample lacks hot dwarf stars in the temperature range $7000 < T_{\text{eff}} < 8000$ K and $4.0 < \log g < 4.5$ because their EW_{862} uncertainties are too high due to their high $v_{\text{sin}i}$ and therefore large uncertainties in their stellar parameters (see Sect. 3). A specific treatment of those stars is necessary but is beyond the scope of this work.

5. Correlation with dust extinction

As mentioned in Sect. 1, the DIB $\lambda 862$ shows a strong correlation with measurements of interstellar reddening such as $E(B - V)$ (e.g., Munari et al. 2008, Wallerstein et al. 2007, Kos et al. 2013). Here, we use the interstellar reddening $E(\text{BP} - \text{RP})$ derived from GSP-Phot as our main dust extinction tracer for individual objects. GSP-Phot provides a detailed characterisation of single stars based on their BP/RP spectra, including stellar parameters (T_{eff} , $\log g$, $[\text{M}/\text{H}]$) and extinction A_0 . We refer to Andrae et al. (2023) for a detailed description of the GSP-Phot module. Due to the extensive filtering in GSP-Phot, only 66 144 stars in our sample have $E(\text{BP} - \text{RP})$ measurements from GSP-Phot. Figure 6 compares the distribution on the sky of the median EW_{862} of the DIB $\lambda 862$ with the median $E(\text{BP} - \text{RP})$. Overall, we see similarities between these two maps, with both showing larger values in the Galactic plane. Nevertheless, we also see some differences: (i) The DIBs $\lambda 862$ seem to be generally more concentrated towards the galactic plane compared to the interstellar dust (see also Sect. 6.2). (ii) In the inner Galaxy

($|\ell| < 30^\circ$), DIBs $\lambda 862$ show a larger scale height compared to the interstellar dust. (iii) We notice at around $\ell \sim 30^\circ$ a low average EW_{862} of the DIB $\lambda 862$ compared to the high amount of dust. This region covers several highly massive star forming regions which were recently surveyed by the GLOSTAR Galactic plane survey in the frequency range between 4 and 8 GHz (Brunthaler et al. 2021). (iv) In the Galactic anticentre region ($|\ell| > 160^\circ$), some specific asymmetric tails of the DIB $\lambda 862$ carrier are visible (see third panel of Fig. 6), reaching large Galactic latitudes ($b < -30^\circ$), which, interestingly, are absent in the northern hemisphere. A detailed comparison between the correlation of interstellar dust and the DIB $\lambda 862$ carrier along certain lines of sight is now possible thanks to the full sky coverage of *Gaia* together with the distances; this should be further investigated.

5.1. EW_{862} versus $E(\text{BP} - \text{RP})$

Figure 7 shows the correlation between $E(\text{BP} - \text{RP})$ and EW_{862} . We see the expected trend between EW_{862} and $E(\text{BP} - \text{RP})$ with a Pearson correlation coefficient (PCC) of 0.68 (the red circles with the uncertainty bars show the corresponding median values and their standard deviation). A linear fit through the median points (indicated by the red line in Fig. 7) is given by

$$E(\text{BP} - \text{RP}) = 4.507(\pm 0.137) \times EW_{862} - 0.026(\pm 0.047). \quad (4)$$

However, stars that were classified as hot stars by GSP-Phot but as cool stars by GSP-Spec deviate from this relation – as indicated by the black open circles in Fig. 7 – in the sense that $E(\text{BP} - \text{RP})$ is too high compared to the measured DIB EW_{862} . Due to the degeneracy between temperature and extinction (see Andrae et al. 2023), the temperatures of those stars are overestimated by GSP-Phot, leading to overestimation of $E(\text{BP} - \text{RP})$. The DIB EW_{862} can therefore be used to find outliers of $E(\text{BP} - \text{RP})$ measurements.

For highly extinguished regions, the EW_{862} of the DIB $\lambda 862$ should become smaller with increasing interstellar reddening and thus depart from a linear relation. Lan et al. (2015) attributed this behaviour to the ‘skin effect’, noting that the DIB strength per unit reddening depends on cloud opacity. Adamson et al. (1991) suggested that the DIB carriers must concentrate in the surface layers (‘skin’) of the clouds and that the carrier depletion might be related to the reduction of the radiation field in the cloud interiors. Adamson et al. (1994) observed this effect with the NIR DIB, something that was later confirmed by Elyajouri & Lallement (2019) for the APOGEE DIB in the dense cores of the Taurus, Orion, and Cepheus clouds. We do not see this effect in our sample, which could be due to a selection effect in the sense that the *Gaia* RVS selection function does not trace the most extinguished regions.

5.2. EW_{862} versus $E(B - V)$

$E(B - V)$ is the most frequently used reddening indicator to study the correlation with DIB strength, especially in early works. To compare our DIB–extinction relation to literature values, we derived the $E(B - V)/EW_{862}$ coefficients from three dust extinction maps: Planck Collaboration Int. XLVIII (2016), Schlegel et al. (1998), and Green et al. (2019). We calculated $E(B - V)$ from the three maps using the Python package *dustmap* (Green 2018).

Planck Collaboration Int. XLVIII (2016) produced a full-sky two-dimensional extinction map using a generalised wavelet

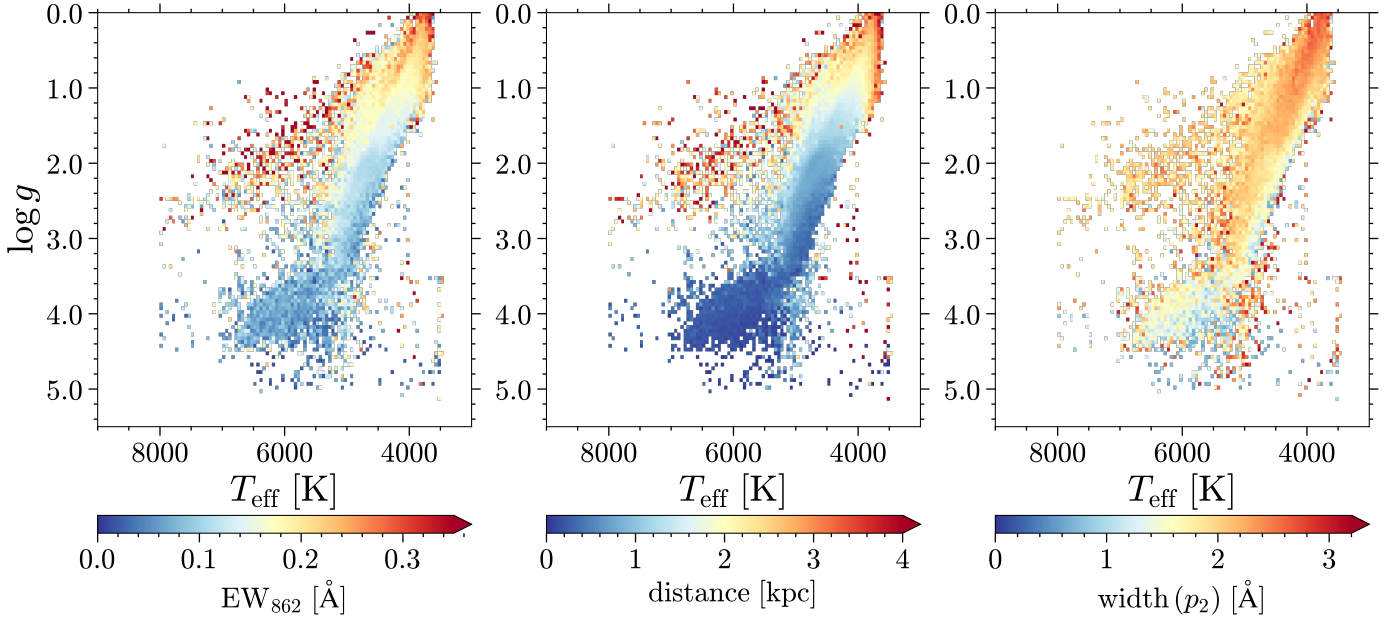


Fig. 5. Mean EW_{862} (left panel), heliocentric photogeometric distance from Bailer-Jones et al. (2021; middle panel), and the width (p_2 , right panel), calculated in $50 \text{ K} \times 0.05 \text{ dex}$ bins, as a function of the Kiel diagram, respectively.

method to separate out Galactic dust emission from cosmic infrared background anisotropies. Such $E(B-V)$ values are asymptotic values and therefore represent overestimations for many of our objects (see Fig. 8b). This also applies to Schlegel et al. (1998; Fig. 8c). Nonetheless, $E(B-V)$ derived from both of these maps for our objects present linear relations with EW_{862} with very high Pearson coefficients. For both Planck Collaboration Int. XLVIII (2016) and Schlegel et al. (1998), we limit their $E(B-V)$ to values smaller than 2.6 mag and get 121 627 and 123 175 individual measurements, respectively. We make use of 55 252 available $E(B-V)$ values from GSP-Phot with a temperature difference between GSP-Spec and GSP-Phot of smaller than 5000 K. Limited by the sky coverage, only 93 247 objects have $E(B-V)$ from Green et al. (2019), a three-dimensional dust reddening map inferred from 800 million stars with Pan-STARRS1 and 2MASS photometry. Based on Schlafly & Finkbeiner (2011), we apply a recalibration factor of 0.884 for $E(B-V)$ from Schlegel et al. (1998). We also use this factor to convert the reddening unit of Green et al. (2019) to $E(B-V)$. We note that the three-dimensional nature of the dust reddening maps from GSP-Phot (Fig. 8a) and from Green et al. (2019; Fig. 8d) negates the problem of overestimated $E(B-V)$ values. Table 3 lists the $E(B-V)/EW_{862}$ coefficients and intercepts derived in this work together with values from the literature.

Figure 8 shows the correlation between EW_{862} and $E(B-V)$ as well as their corresponding linear fits. We notice a large variation in the derived $E(B-V)/EW_{862}$, which is due to the use of different methods for extinction calculation, with a very high value of 4.128 ± 0.062 from Planck Collaboration Int. XLVIII (2016) and a low value of 2.198 ± 0.066 from Green et al. (2019). It is not surprising that different works report different values for the ratio of $E(B-V)/EW_{862}$, depending on the sightlines studied and the techniques applied for DIB and extinction measurements. The high coefficients with $E(B-V)$ from Schlegel et al. (1998) and Planck Collaboration Int. XLVIII (2016) imply that extinction measured from infrared emission is not only overestimated in some regions but presents systematic differences (larger values) compared to the values calculated using other methods.

Table 3. Coefficients and intercepts of the linear relations between DIB $\lambda 862$ and $E(B-V)$ derived in the literature and this work.

Works	$E(B-V)/EW_{862}$ (mag \AA^{-1})	Intercept
This work	3.016 ± 0.047 ^(a)	0.023 ± 0.013
	4.128 ± 0.068 ^(b)	0.021 ± 0.019
	4.031 ± 0.060 ^(c)	-0.013 ± 0.017
	2.198 ± 0.066 ^(d)	-0.004 ± 0.019
Sanner et al. (1978)	2.85 ± 0.11 ^(e)	–
Munari et al. (2008)	2.72 ± 0.03	–
Wallerstein et al. (2007)	4.61 ± 0.56	–
Kos et al. (2013)	2.49 ± 0.23	0.028 ± 0.002
Puspitarini et al. (2015)	2.12 ^(f)	–
Królowski et al. (2019)	2.03 ± 0.15	0.22 ± 0.05
Zhao et al. (2021b)	3.460 ± 0.313	-0.015 ± 0.060

Notes. ^(a) $E(B-V)$ from GSP-Phot. ^(b) $E(B-V)$ from Planck Collaboration Int. XLVIII (2016). ^(c) $E(B-V)$ from Schlegel et al. (1998). ^(d) $E(B-V)$ from Green et al. (2019). ^(e)Calculated by Kos et al. (2013). ^(f)Estimated by their Fig. 7.

5.3. Hot stars

In addition to the results obtained by GSP-Phot and GSP-Spec, the Apsis pipeline also contains the ESP-HS (Extended Stellar Parametrizer for Hot Stars) which specifically processes the BP/RP and RVS data for stars hotter than 7500 K (Gaia Collaboration 2022). The module provides the astrophysical parameters of O-, B-, and A-type stars, including an estimate of the interstellar extinction (A_0 , A_G), and reddening $E(\text{BP-RP})$. The target overlap between GSP-Phot, GSP-Spec, and ESP-HS is small due to the post-processing filtering and quality assessment of the module, their T_{eff} validity domain (e.g., main valid AP domain of GSP-Spec is $T_{\text{eff}} < 8000 \text{ K}$), and/or parameter degeneracy. Keeping this in mind, there are 2929 ESP-HS hot stars with an estimate of the DIB EW_{862} , and only 1142 that

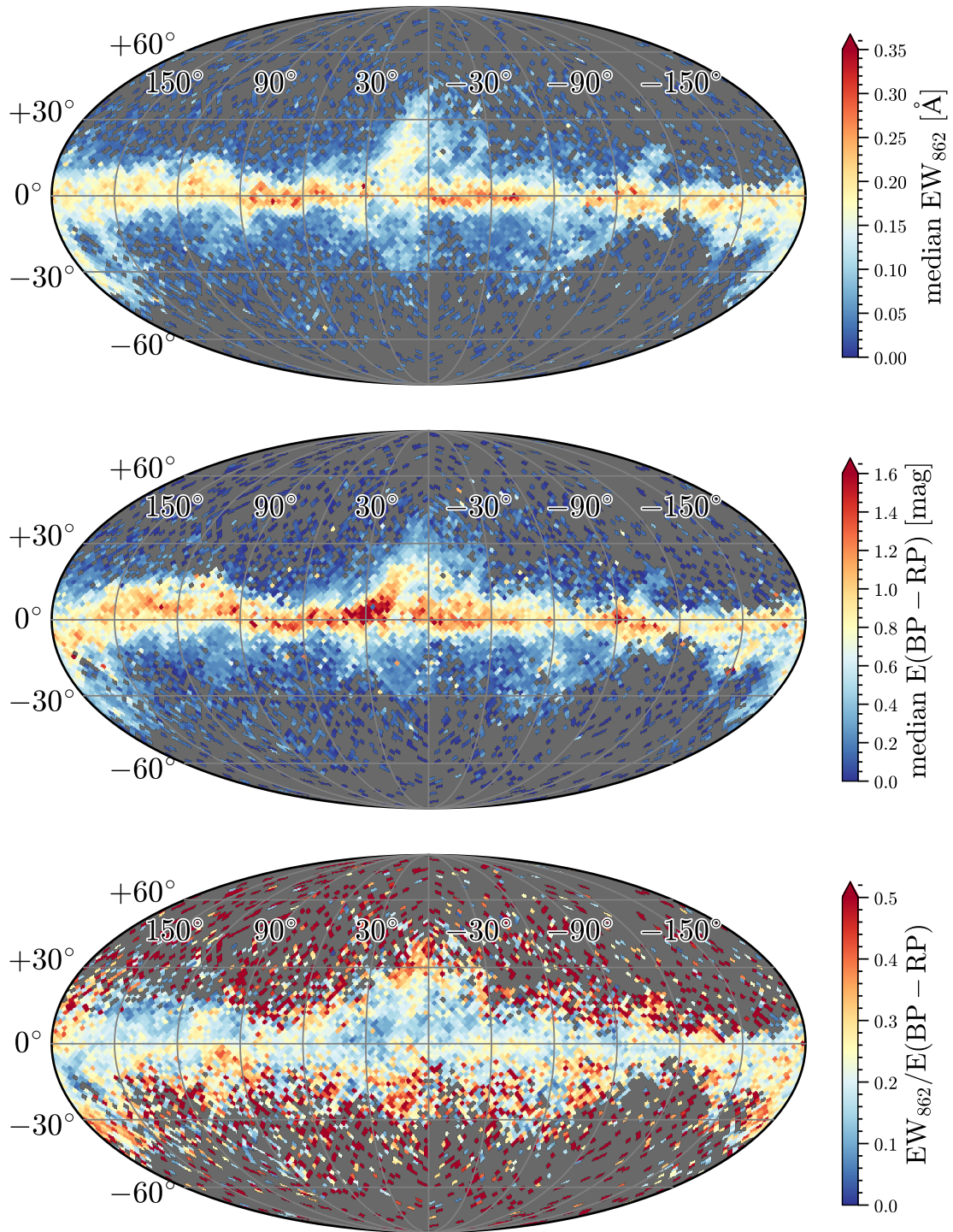


Fig. 6. Comparison between the median EW_{862} of the DIB $\lambda 862$ (*upper panel*), the median $E(BP - RP)$ (*middle panel*), and the ratio $EW_{862}/E(BP - RP)$ (*lower panel*) at HEALPix level 5 in the Mollweide projection.

belong to the HQ sample. In the upper panel of Fig. 9, we plot the interstellar reddening against the DIB EW_{862} for the latter sample, which provides a Pearson correlation coefficient (PCC) of +0.69. Eight outliers were identified. A brief description of these is provided in Table C.1 (8 upper rows).

The hottest stars (labelled 1–3 in Fig. 9) are targets cooler than 7500 K (according to GSP-Spec), and those that were treated with non-adapted synthetic spectra by ESP-HS. Outlier ‘7’ is known from Simbad (Wenger et al. 2000) to exhibit

emission. On the other hand, the $H\alpha$ pseudo-EW provided by the ESP-ELS module is positive (i.e. no significant emission is found in $H\alpha$ from the BP/RP spectrum), and its RVS spectrum appears normal. It therefore remains unclear as to why the derived APs (which include the extinction) do not provide a correct fit to the data. Outlier ‘6’ has a very peculiar RVS spectrum belonging to an extreme He star (FQ Aqr). Outliers ‘4’, ‘5’, and ‘8’ show good agreement between observed and RVS fitted spectra.

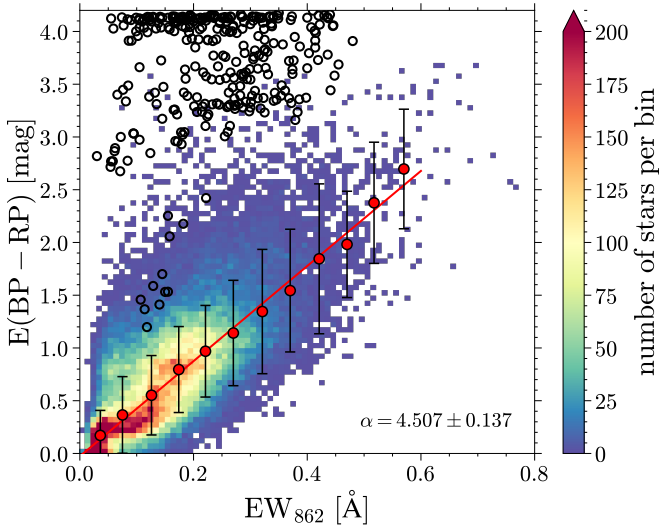


Fig. 7. Correlation between EW_{862} and $E(\text{BP} - \text{RP})$ for 55 557 measurements in the high-quality sample with $E(\text{BP} - \text{RP})$ values. The colour scale shows the number of stars per $0.01 \text{ \AA} \times 0.05 \text{ mag}$ bin. The red dots are the median values taken in EW_{862} bins from 0 to 0.6 \AA with a step of 0.05 \AA . The red line is the linear fit to the red dots. The fitting gradient and its uncertainty are also indicated. The open black circles (305 in total) are sources with a temperature difference (GSP-Phot – GSP-Spec) larger than 5000 K.

A similar trend is observed in the GSP-Phot vs. GSP-Spec data, and plotted in the two lower panels of Fig. 9. In the middle panel, the selection is solely based on the effective temperature provided by GSP-Spec. Targets with a DIB EW_{862} of greater than 0.5 \AA are identified and numbered (Table C.1). With the exception of the star labelled ‘6’, which shows an RVS spectrum typical for an early-B or late-O star, all the stars have spectral features usually seen in M or late-K-type stars (which is confirmed by Simbad in two cases; in the other ones no additional information was found). Therefore, these are confirmed outliers, and to consistently (e.g., between the two GSP modules) remove those points, we performed a second selection based on the T_{eff} derived by both modules ($T_{\text{eff}} > 7000 \text{ K}$). This last selection is plotted in the lower panel of Fig. 9, and provides a $\text{PCC} = +0.77$. The first selection attempt (middle panel) provides a median $E(\text{BP} - \text{RP})$ versus EW_{862} that is slightly lower than the relation obtained for the cooler stars (represented by the broken blue line), while the first and third ones are in fair agreement with this latter. The sample combination of the ESP-HS and GSP-Phot/GSP-Spec (Fig. 9, lower panel) selections provides 1 804 hot stars.

5.4. Comparison with the TGE dust map

The total galactic extinction (TGE) map is a full-sky 2D representation of the foreground extinction from the Milky Way towards extragalactic sources, which is constructed from selected sources at large distances beyond the Galactic disk. To derive this map, distant giants were selected in order to obtain a set of stars situated beyond the dust layer of the disk of the Galaxy. The median of extinctions derived by GSP-Phot was then used to assign an extinction value for each HEALPix at different levels. For further details on the TGE maps, see Delchambre et al. (2023).

In the following, we use the HQ DIB sample as defined in Sect. 3. In order to compare the EW_{862} of the DIB $\lambda 862$ to the TGE map, it is first necessary to construct a HEALPix map of the EW_{862} in the same way as for the TGE map. We selected the DIB $\lambda 862$ DIB EW_{862} measurements based on their Galactic altitude ($|z| > 300 \text{ pc}$) and then calculated the median EW_{862} in each HEALPix. Only HEALPixels with more than one DIB $\lambda 862$ measurement were retained.

The resulting DIB EW_{862} HEALPix map is shown at level 5 in Fig. 10 (top left panel). We note that, due to our selection of DIB $\lambda 862$ sources, this figure is not the same as the top panel of Fig. 6. Also shown in the top right panel of Fig. 10 is the TGE map at level 5, where the value of a level-5 superpixel is the mean of the four level-6 pixels. Any level-5 HEALPix containing at least one level-6 HEALPix with insufficient tracers (less than three) is flagged as having no data. The lower left panel of Fig. 10 shows the resulting sky map of the EW_{862}/A_0 ratio, and the lower right panel shows a scatter plot of EW_{862} as a function of TGE A_0 . Although the DIB $\lambda 862$ map does not cover the entire sky (due to a lack of sufficient tracers), the two maps trace the same large-scale structures across the sky. The ratio of the two values is fairly constant from low to mid Galactic latitudes, but large fluctuations are seen at higher latitudes where the number of tracers drops considerably. The scatter plot shows good correlation between the two values up to an A_0 of 1.5 mag , after which the EW_{862} rises more slowly than the TGE A_0 . This is a consequence of the fact that A_0 traces asymptotic values of extinction which (in the highly extinct regions) may occur beyond the distance of stars observed in DIB $\lambda 862$ measurements. A straight line fit to the scatter plot (broken line) below 1.5 mag results in a slope of 0.07 and an intercept of 0.03 .

6. Spatial distribution of the DIB $\lambda 862$

Figure 11 shows a full sky map of the median values of the integrated EW_{862} of the DIB $\lambda 862$ for the whole HQ sample, taken from $0.1 \text{ kpc} \times 0.1 \text{ kpc}$ bins in XY , XZ , and YZ planes, respectively. Stellar photogeometric distances are those from Bailer-Jones et al. (2021). The overall distribution is similar to the pseudo-3D map (Kos et al. 2014) from RAVE data (Steinmetz et al. 2020), although a larger number of sight lines and coverage over the whole sky with *Gaia* DR3 allow us to draw more specific conclusions.

First, we note that EW_{862} increases with distance. This is expected, but it is a nice validation of our results, as this increase was not assumed when measurements of the DIB $\lambda 862$ were made. The two cross-sections perpendicular to the Galactic plane in Fig. 11 show that DIB $\lambda 862$ carriers are largely confined to the Galactic plane, as expected. We note that the regions with strong DIBs $\lambda 862$ in two directions away from the plane (seen in the YZ cross-section) start locally and do not increase in intensity with distance. They therefore originate in clouds of DIB $\lambda 862$ carriers which reside close to the Sun and cause DIB $\lambda 862$ absorption in spectra of all stars located behind them.

The XY panel of Fig. 11 suggests that stars within spiral arms generally show stronger EW_{862} of the DIB $\lambda 862$ carriers. This is true for the Scutum–Centaurus arm and for the Perseus arm. Our map lacks the reach needed to claim the same for the Outer arm, though an increase of DIB $\lambda 862$ intensity at a distance of $\sim 4 \text{ kpc}$ in the Galactic anticentre direction agrees with this conjecture. The situation for the Local arm and the Sagittarius–Carina arm is more complicated: a region with strong DIBs $\lambda 862$ at $\ell \simeq 60^\circ$ coincides with the spur between these two arms (indicated by the blue line in Fig. 11). However, there is also an indication of a region of

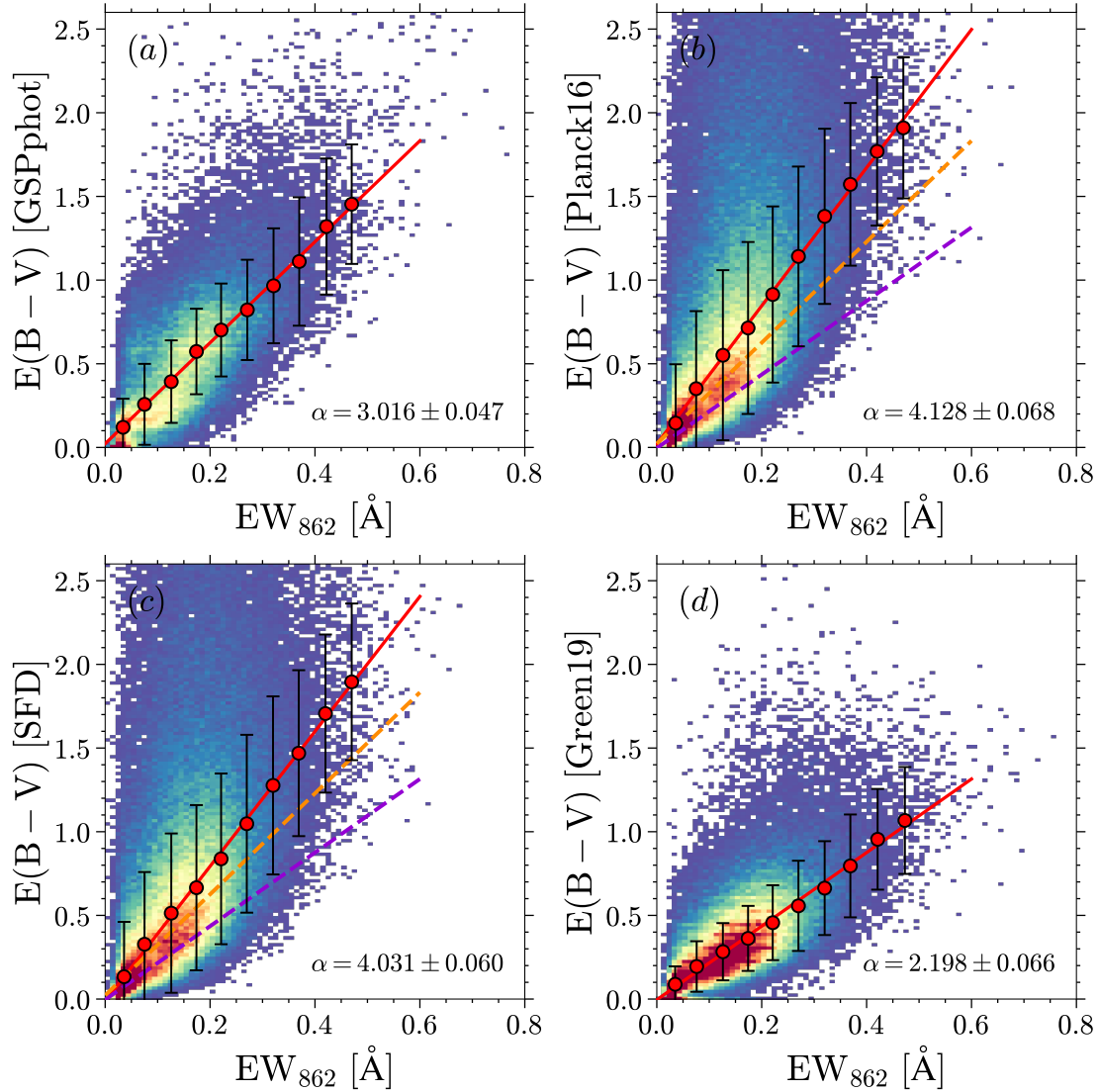


Fig. 8. Correlations between EW_{862} and $E(B - V)$ derived from different extinction maps: (a) GSP-Phot, (b) Planck Collaboration Int. XLVIII (2016), (c) Schlegel et al. (1998), and (d) Green et al. (2019). The colours in each panel show the target number per $0.01 \text{ \AA} \times 0.02 \text{ mag}$ bin. The colour bar is the same as in Fig. 7. The red circles are the median values taken in EW_{862} bins from 0 to 0.5 \AA with a step of 0.05 \AA . The red lines are linear fits to the red dots in each panel, respectively. The fitting gradients (α) and their uncertainties are indicated. They are also listed in Table 3. The orange and violet dashed lines in (b) and (c) are the fit results to GSP-Phot and Green et al. (2019), respectively.

strong DIBs $\lambda 862$ in the opposite direction, at $\ell \approx 270^\circ$. This may indicate that DIBs $\lambda 862$ fill in the region between the Sagittarius–Carina and Local arms, with the exception of a large void around the Solar position. However, we note that we do not claim the DIB carrier clouds are seen to reside within the spiral arms, as the presence of the Local Bubble around the Sun amplifies a general rise of EW with distance in any direction along the Galactic plane. A detailed investigation of the spatial distribution of DIB carriers is beyond the scope of this paper and will be discussed in Zhao et al. (in prep.).

Figure 12 compares the spatial distribution of DIB $\lambda 862$ and dust absorptions. We note that only 40% of the DIB $\lambda 862$ sample has valid $E(\text{BP} - \text{RP})$ measurements due to a strong quality filtering in GSP-Phot. The comparison therefore only refers to 55 080 sources in common and not to the whole DIB $\lambda 862$ HQ sample shown in Fig. 11. The top panels show the distribution of the colour excess, and the bottom panel is the ratio between EW_{862} and $E(\text{BP} - \text{RP})$ with a subtracted linear fit from Fig. 7.

Two important results of Figs. 11 and 12 are that the spatial distribution of DIB $\lambda 862$ carriers and dust are qualitatively similar, but their ratio shows a pronounced lack of dust absorption for nearby sight lines. The red regions in the bottom panels of Fig. 12 demonstrate that the Local Bubble around the Sun which contains very little dust does not have a similar low density of DIB $\lambda 862$ carriers. This is confirmed with a median $EW_{862} \sim 0.1 \text{ \AA}$ within the inner 150 pc from the Sun. To investigate the situation further, Fig. 13 shows a zoom into the $4 \times 4 \times 0.6 \text{ kpc}$ rectangular box centred on the Sun for stars that have valid EW_{862} and $E(\text{BP} - \text{RP})$ measurements. In addition, the positions of the nearby molecular clouds from Zucker et al. (2020) are indicated by dots: black for clouds within 100 pc from the plane and red for those at heights between 100 and 300 pc. It is encouraging to see that molecular clouds at low Galactic heights are indeed at the head of strong DIB $\lambda 862$ directions and dust absorptions in the XY plane. This suggests that the light from behind stars passes through these clouds of

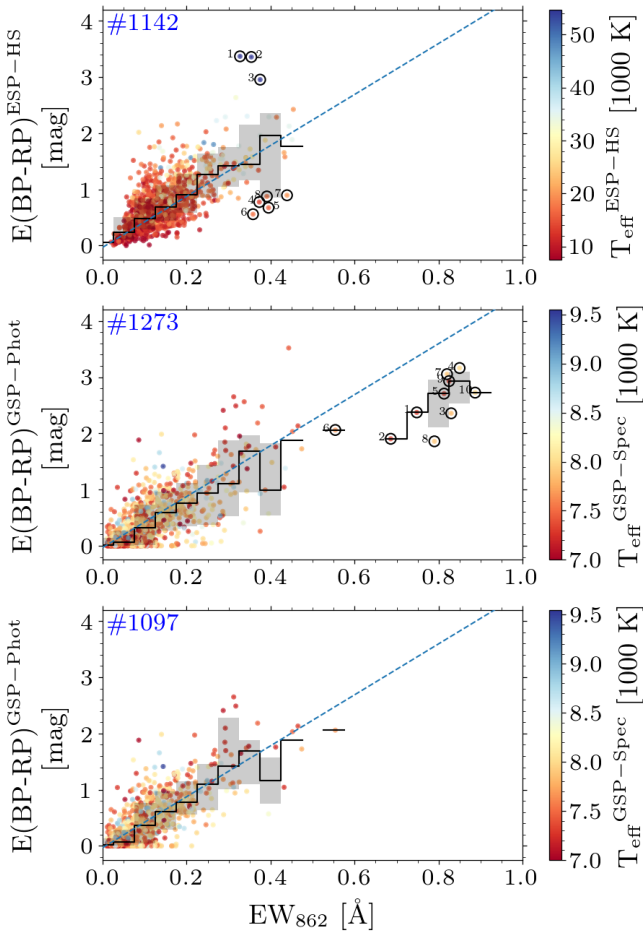


Fig. 9. $E(\text{BP} - \text{RP})$ vs. EW_{862} of the DIB $\lambda 862$ derived for the HQ sample by GSP-Spec for *hot* stars. The colour code follows the effective temperature derived by ESP-HS or GSP-Spec. The running median and interquartile (15–85%) are represented by a black step curve and the shaded area, respectively. The relation derived for the cooler stars is shown by the broken blue line. *Upper panel:* reddening derived using the ESP-HS module for stars hotter than 7500 K. The outliers are identified with black circles and numbers. *Middle panel:* $E(\text{BP} - \text{RP})$ from GSP-Phot for targets hotter than 7000 K according to GSP-Spec only. *Lower panel:* $E(\text{BP} - \text{RP})$ from GSP-Phot, and hotter than 7000 K according to GSP-Spec and GSP-Phot. Numbered black circles denote the outliers which are discussed in the main text, with their parameters listed in Table C.1.

simple molecules, dust, and DIB $\lambda 862$ carriers and so their volume-filling factor is large enough for this to happen. Similarly, molecular clouds at larger distances from the Galactic plane (red dots) seem to correspond to directions of enhanced dust absorption and DIB $\lambda 862$ presence away from the plane.

We note that Figs. 11 and 12 are based on the assumption of a Gaussian profile for the DIB carrier. The profile of the DIB may be more complicated or may vary in shape; in some cases one may expect a superposition of absorptions originating in multiple clouds along the line of sight, but the EW_{862} values we derive are not affected significantly, as long as the radial velocities of the DIB carriers and profile variations are small compared to the width of the profile in our spectra with a moderate resolving power. The EWs we derive are always small, and so we are in a linear regime where the total value is a simple sum of individual absorptions. In addition, the departures from the Gaussian profile caused by the superposition effect have been shown to

be insignificant for DIB $\lambda 862$ by comparing the fitted EW with the integrated EW (Kos et al. 2013) and EW calculated from an asymmetric Gaussian function (Zhao et al. 2021a).

Due to the large catalogue of DIB $\lambda 862$, and the better sampling for different sightlines, we can trace the spatial variation of $\text{EW}_{862}/E(\text{BP} - \text{RP})$ (bottom in Fig. 12) which can be used as a tracer to reveal the local physical conditions; as in the work of Vos et al. (2011) for the Scorpius OB2 association. The ultimate goal would be to compare the densities of dust and DIB $\lambda 862$ carrier derived by extinction and EW, respectively. A series of works carried out such a comparison for the dust (e.g., Capitanio et al. 2017; Rezaei Kh et al. 2018; Lallement et al. 2014, 2019; Rezaei Kh et al. 2020). No attempt has been made so far for DIB $\lambda 862$.

A detailed analysis of the spatial co-location of molecular clouds and clouds of DIB $\lambda 862$ carriers and interstellar dust, together with a study of their spatial filling factors, is beyond the scope of this paper and will be explored in the future.

6.1. The Local Bubble

Farhang et al. (2019) studied the low-density cavity known as the Local Bubble and found the presence of the DIB carriers at $\lambda 5797$ and $\lambda 5780$ in the bubble. Other detailed studies of the local ISM were obtained from Vergely et al. (2001, 2010), Welsh et al. (2010). Figure 14 shows the distribution of the DIB $\lambda 862$ carrier in the inner 300 pc volume with respect to the Sun within 100 pc from the Galactic plane. In the left-hand panel, a clear asymmetry can be seen in the distribution of the DIB $\lambda 862$, which is also seen in other DIB maps in the Local Bubble (see e.g., Farhang et al. 2019, Bailey et al. 2016), while in the inner 100 pc we see a homogeneous distribution of weak DIBs ($\text{EW} < 0.05 \text{ \AA}$).

Figure 14 shows the correlation of the DIB $\lambda 862$ of our sample with the dust extinction derived from $E(\text{BP} - \text{RP})$. Here, we see a clear linear relation in this extreme low-extinction region even for very small EW ($< 0.05 \text{ \AA}$). However, a more detailed discussion of the behaviour of the DIB $\lambda 862$ in the Local Bubble is beyond the scope of this paper.

6.2. Scale height

To characterise the vertical distribution of the carrier of the DIB $\lambda 862$, we assume an exponential model and follow the straightforward method used in Kos et al. (2014). Following this approach, the DIB strength EW_{862} and the stellar distance (d) in a narrow latitude slab can be derived as

$$\text{EW}_{862} = \int_0^d \rho_0 \exp\left(\frac{-s \sin(|b|)}{z_0}\right) ds + B = A [1 - \exp(-d/d_0)] + B, \quad (5)$$

where z_0 is the scale height, b is the galactic latitude, d is the heliocentric distance, $d_0 = z_0/\sin(|b|)$, $A = \rho_0 z_0/\sin(|b|)$, and B is a small offset of our EW_{862} values due to the fact that only sufficiently strong DIBs $\lambda 862$ pass the selection criteria for the HQ sample. So that we can compare the data points at different latitudes, we follow Kos et al. (2014) and first normalise the curves in different latitude bins by fitting parameters $((\text{EW}_{862} - B)/A)$. This normalised EW_{862} is then fitted again by Eq. (5) in order to get the scale height z_0 . We refer to Kos et al. (2014) for more details, especially their Fig. 2.

Kos et al. (2014) applied this method for 20 latitude slabs from $b = -20^\circ$ to $b = 20^\circ$ with a bin size of 2° and obtained

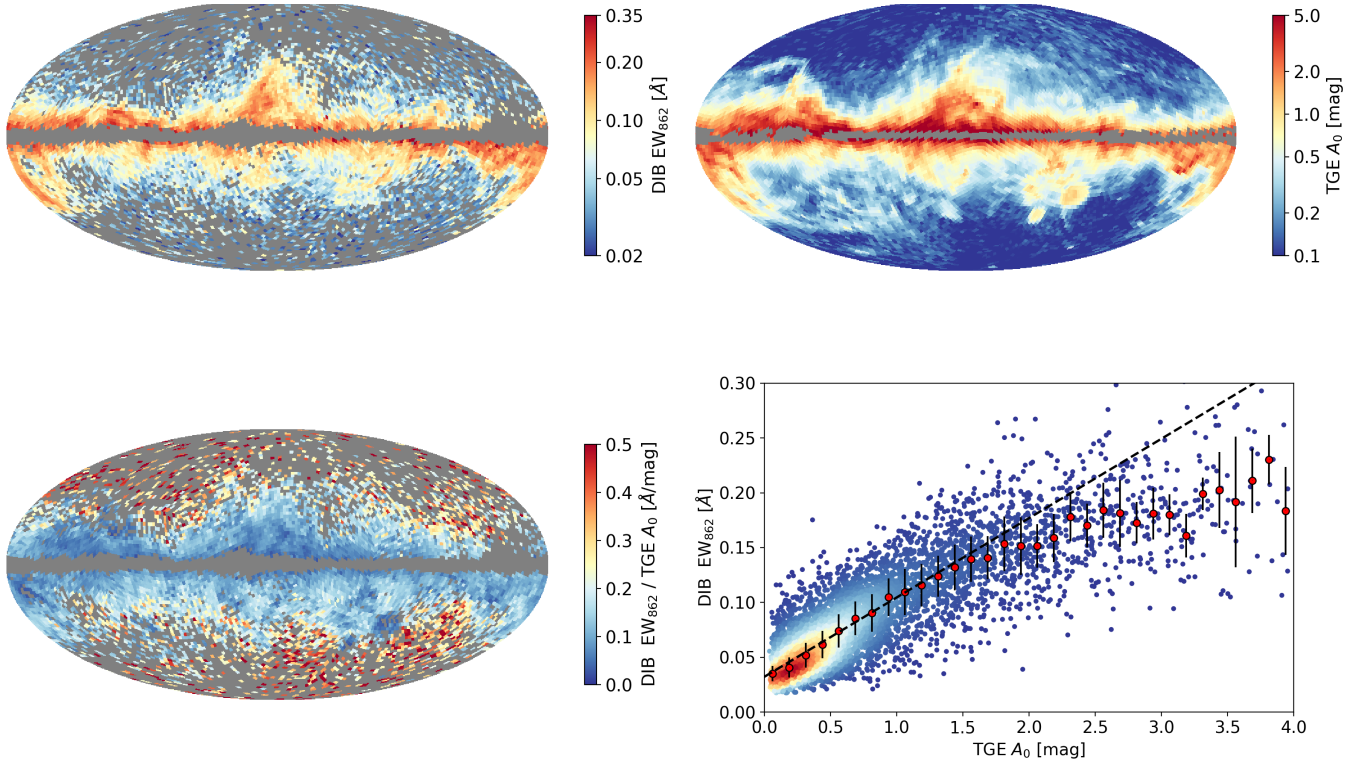


Fig. 10. *Top left:* EW_{862} of the HQ sample for stars beyond the Galactic disk ($|z| > 300$ pc), averaged in each level-5 HEALPix. Grey pixels indicate no data, where there are fewer than two DIB $\lambda 862$ measurements in the level-5 HEALPix. *Top right:* TGE A_0 at HEALPix level 5, again where grey signifies no data (i.e. where there are insufficient extinction tracers). *Bottom left:* EW_{862} vs. TGE over the sky. *Bottom right:* density plot of EW_{862} vs. TGE. The median EW_{862} in regular TGE bins is shown as red points. The uncertainty bars are derived using the average absolute deviation around the median.

$z_0 = 209.0 \pm 11.9$ pc. We only use eight slabs with moderate latitudes ($-12^\circ \leq b \leq -4^\circ$ and $4^\circ \leq b \leq 12^\circ$) which show exponential saturation, and take median EW_{862} in each 0.25 kpc bin from 0 to $d = 3$ kpc. To compare with the result of Kos et al. (2014), we first consider measurements with $240^\circ \leq \ell \leq 330^\circ$ (upper panel in Fig. 15). The normalised EW_{862} with $z > 0.4$ kpc show an apparent offset due to the low quality of the fitting at large distances from the Galactic plane. Therefore, we only fit the data points with $|z| \leq 0.4$ kpc by Eq. (5) and get $z_0 = 133.15^{+4.71}_{-4.32}$ pc, which is a smaller value than that derived by Kos et al. (2014). We note that we do not survey the same sample here and that Kos et al. (2014) had to resort to averaging of DIB $\lambda 862$ measurements from different stars, meaning that their sample may be influenced by systematic errors in distance measurements available in the pre-Gaia era.

Gaia makes an all sky survey of DIBs $\lambda 862$ which is not restricted to the Southern hemisphere and equatorial region, as is the case for RAVE. Using all available lines of sight (lower panel in Fig. 15), the fitted z_0 decreases to $98.69^{+10.81}_{-8.35}$ pc. The uncertainties are small and may indicate a variation of the DIB $\lambda 862$ scale height on the line of sight. This is consistent with the spatial distribution of the DIBs $\lambda 862$ (see Fig. 6) where we notice, for example, a larger z_0 for the inner disc ($|\ell| < 30^\circ$). Our derived z_0 of the DIB $\lambda 862$ carrier towards all available lines of sight with $4^\circ \leq |b| \leq 12^\circ$ is close to the scale height of the carrier of the DIB at $1.527 \mu\text{m}$ derived by Zasowski et al. (2015) with $z_0 = 108 \pm 8$ pc but is slightly smaller than the scale height of the dust grains as measured by various authors, such as 134.4 ± 8.5 pc by Drimmel & Spergel (2001), 125^{+17}_{-7} pc by Marshall et al. (2006), 119 ± 15 pc by Jones et al. (2011). On the other hand, Li et al. (2018) reported a smaller value of 103 pc while Guo et al. (2021)

obtained two z_0 , 72.7 ± 2.4 pc and 224.6 ± 0.7 pc, for a two-disk model. For comparison, dense molecular gas such as ^{12}CO has a smaller scale height of $\sim 50\text{--}70$ pc (Sanders et al. 1984). For stars with $4^\circ \leq |b| \leq 12^\circ$, we derive $\rho_0 = 0.19 \pm 0.04 \text{ \AA kpc}^{-1}$ and $B = 0.05 \pm 0.01 \text{ \AA}$. This allows the reader to use Eq. (5) as an estimate of the expected DIB $\lambda 8620$ carrier strength towards any star in the solar neighbourhood with $4^\circ \leq |b| \leq 12^\circ$. The ratio of the measured EW_{862} over the expected EW_{862} has 16 and 84 percentile values of 0.66 and 1.30. A detailed characterisation of the DIB $\lambda 862$ carrier extending beyond the symmetric models is needed to study local substructures in and out of the Galactic plane.

7. Rest-frame wavelength

One of the most important observational properties of the DIB $\lambda 862$ is its central rest-frame wavelength (λ_0), which is necessary to identify the DIB $\lambda 862$ carrier through comparison to laboratory measurements. A frequently used method is to use the well-identified interstellar atomic or molecular lines to shift the whole spectrum to the rest velocity frame assuming a tight correlation between the DIB $\lambda 862$ and the interstellar lines (e.g., Jenniskens & Desert 1994; Galazutdinov et al. 2000a). Without the interstellar counterpart, λ_0 can also be statistically determined with the empirical assumption that the radial velocity in the Local Standard of Rest (LSR) towards the Galactic centre (GC) or the Galactic anti-centre (GAC) is almost null (e.g., Munari et al. 2008; Zasowski et al. 2015; Zhao et al. 2021b).

We apply this statistical method for both GC and GAC by selecting targets with $\Delta\ell \leq 10^\circ$, $|b| \leq 2^\circ$, $d \leq 4$ kpc, $QF = 0$, $\text{err}(\lambda_c) < 1.0 \text{ \AA}$, and valid stellar radial velocities.

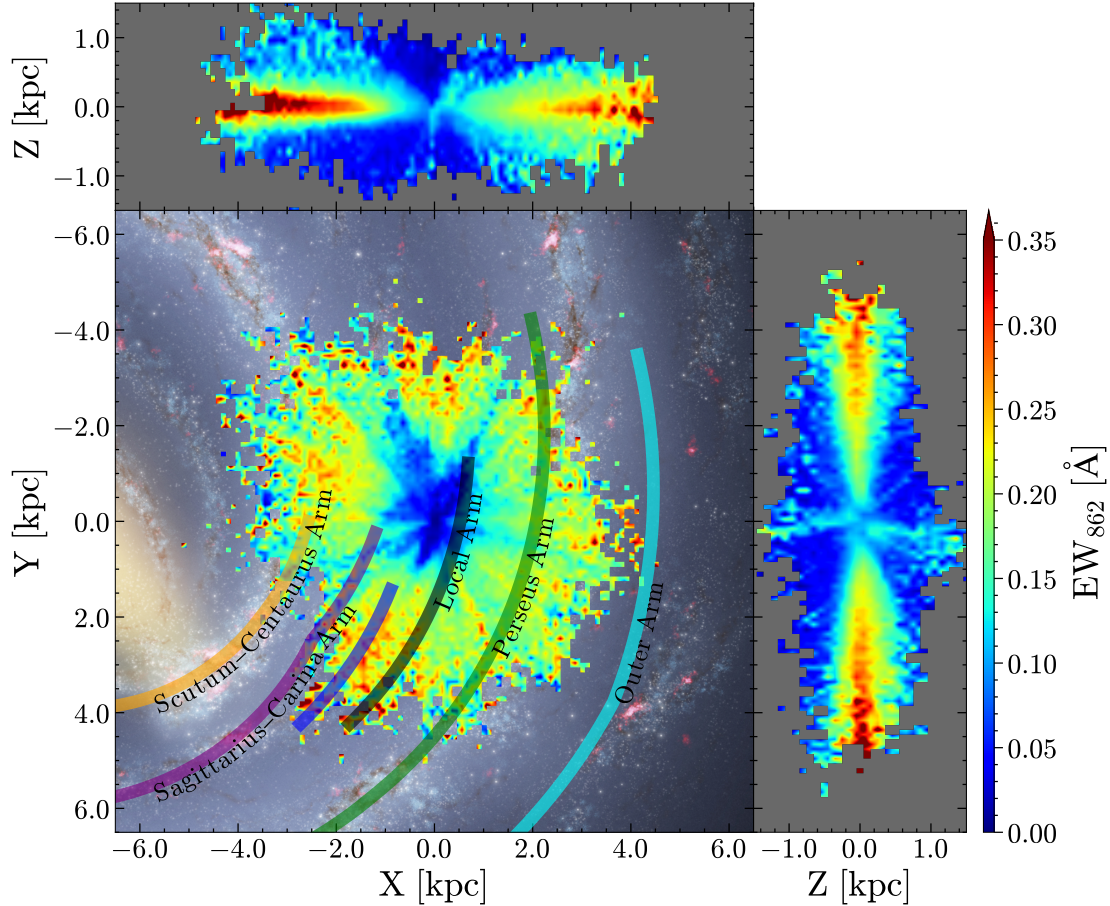


Fig. 11. Face-on and side-on views of the spatial distribution of the DIB $\lambda 862$ for the whole HQ sample plotted over the Milky Way sketch created by Robert Hurt and Robert Benjamin (Churchwell et al. 2009). Median EW_{862} are taken from $0.1 \text{ kpc} \times 0.1 \text{ kpc}$ bins in XY , XZ , and YZ planes, respectively. The Galactic centre is located at $(X, Y, Z) = (-8, 0, 0)$. The coloured lines represent the Galactic log-periodic spiral arms described by the parameters from Reid et al. (2019): Scutum–Centaurus arm, orange; Sagittarius–Carina arm, purple; Local arm, black; Perseus arm, green; Outer arm, cyan. The spur between the Local and Sagittarius–Carina arms is indicated by the blue line.

This provides 1405 stars for GC and 1106 cases for GAC. Figure 16 shows their measured central wavelengths in the heliocentric frame (C_{obs}) as a function of the angular distance from GC and GAC, respectively. By the linear fit to the median values in each $\Delta\ell = 1^\circ$ bin, we get $C_{\text{obs}} = 8623.10 \pm 0.018 \text{ \AA}$ at $\ell = 0^\circ$ and $C_{\text{obs}} = 8623.54 \pm 0.019 \text{ \AA}$ at $\ell = 180^\circ$. We stress that these are vacuum wavelengths, which means they are appropriate for *Gaia* observations. For GAC, C_{obs} increases with Galactic longitude, having a slope of $23 \pm 3.4 \text{ m\AA deg}^{-1}$, while the longitude trend is flatter toward the GC, with a slope of $1.2 \pm 3.1 \text{ m\AA deg}^{-1}$. Fitting with a more constrained longitude region, such as $\Delta\ell \leq 2^\circ$, yields very similar intercepts, that is $C_{\text{obs}} = 8623.10 \pm 0.016 \text{ \AA}$ at $\ell = 0^\circ$ and $C_{\text{obs}} = 8623.52 \pm 0.023 \text{ \AA}$ at $\ell = 180^\circ$. Nevertheless, both of the slopes toward GC and GAC become larger and much closer to each other: $47 \pm 14 \text{ m\AA deg}^{-1}$ for GC and $45 \pm 20 \text{ m\AA deg}^{-1}$ for GAC. These slopes are also consistent with the values of $57 \pm 8 \text{ m\AA deg}^{-1}$ derived by Zasowski et al. (2015) for the DIB at $1.5273 \mu\text{m}$, 47 m\AA deg^{-1} derived from the CO rotation curve (Clemens 1985), and 40 m\AA deg^{-1} derived from the stellar rotation curve (Bovy et al. 2012).

Considering the effect of solar motion, λ_0 in vacuum is derived as $c/(c - U_\odot) \times C_{\text{obs}} = 8623.41 \text{ \AA}$ for GC, and $c/(c + U_\odot) \times C_{\text{obs}} = 8623.23 \text{ \AA}$ for GAC, where c is the speed of the light and $U_\odot = 10.6 \text{ km s}^{-1}$ (Reid et al. 2019) is the radial

solar motion. The difference between them may be caused by non-circular motion of the DIB $\lambda 862$ carrier about the Galactic centre, which makes the LSR velocity non-zero. We believe this systematic effect is less pronounced in the direction of the GAC, and so we use this value to derive its counterpart wavelength in the air of 8620.86 \AA . This number agrees well with our previous result from the Giraffe Inner Bulge Survey (Zoccali et al. 2014) towards the GC (8620.83 \AA ; Zhao et al. 2021b). The obtained value in this work is slightly larger than the values of $8620.70 \pm 0.3 \text{ \AA}$ (Sanner et al. 1978), 8620.75 \AA (Herbig & Leka 1991), and 8620.79 \AA (Galazutdinov et al. 2000b). The result of Jenniskens & Desert (1994), namely $8621.11 \pm 0.34 \text{ \AA}$, is very close to our result towards GC (8621.03 \AA in air). Based on 68 hot stars from RAVE, Munari et al. (2008) measured a mean C_{obs} toward GC as $8620.4 \pm 0.1 \text{ \AA}$, corresponding to a $\lambda_0 = 8620.70 \text{ \AA}$ after the solar-motion correction, which is also smaller than our result. Fan et al. (2019) obtained a much smaller $\lambda_0 = 8620.18 \pm 0.25 \text{ \AA}$, an average value of 17 for their program spectra, which was measured in the averaged optical-depth profiles and corrected by the interstellar KI line at 7699 \AA . The lower quality of their spectra at longer wavelengths and the complex velocity structure of the atomic species could be the cause of the large difference between their results and others (Haoyu, priv. comm.).

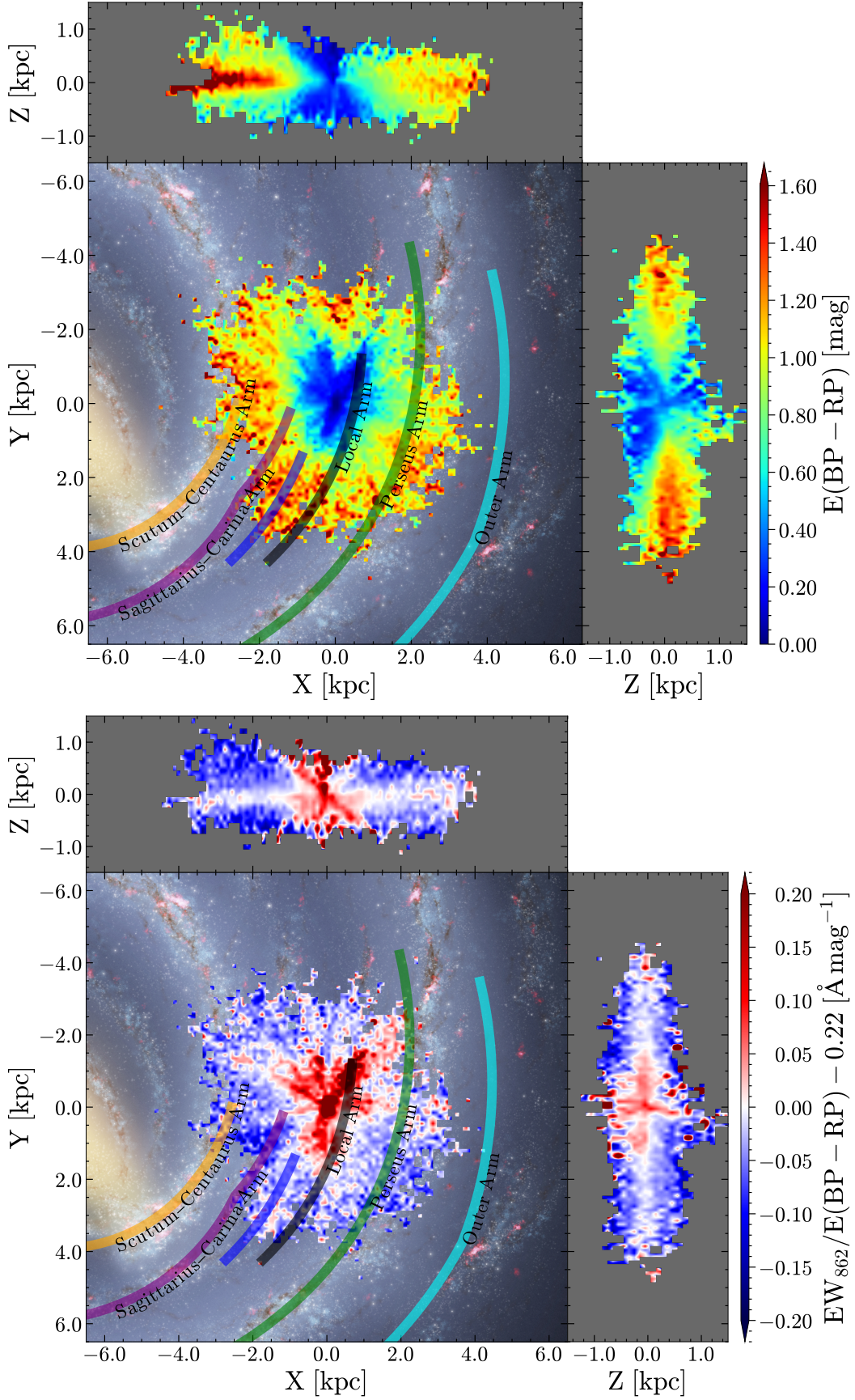


Fig. 12. Same as Fig. 11, but for $E(\text{BP} - \text{RP})$ from GSP-Phot (*upper panel*), and the ratio of $\text{EW}_{862}/E(\text{BP} - \text{RP})$ (*lower panel*), subtracting 0.22, the inverse of the linear gradient fitted in Fig. 7. Only 55 080 sources in the HQ sample with $E(\text{BP} - \text{RP})$ measurements are used.

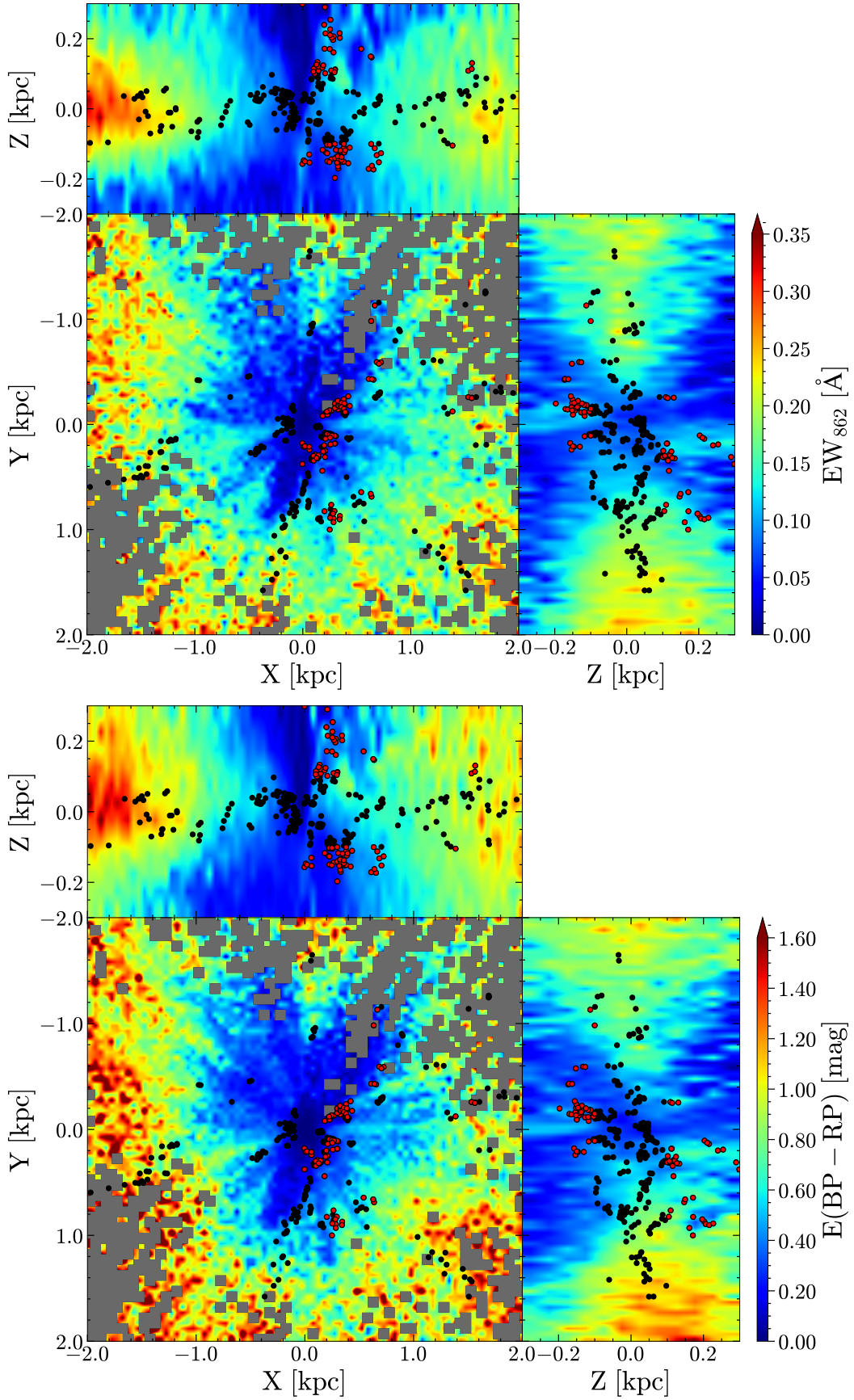


Fig. 13. Same as Fig. 11 but for a subsample containing 39 224 cases with $|X| \leq 2$ kpc, $|Y| \leq 2$ kpc, $|Z| \leq 0.3$ kpc, and valid $E(BP - RP)$. Median EW_{862} are taken from 0.05 kpc \times 0.05 kpc bins in XY , XZ , and YZ planes, respectively. Overplotted are nearby MCs measured in Zucker et al. (2020). The MCs with $Z \geq 0.1$ kpc are indicated as red dots.

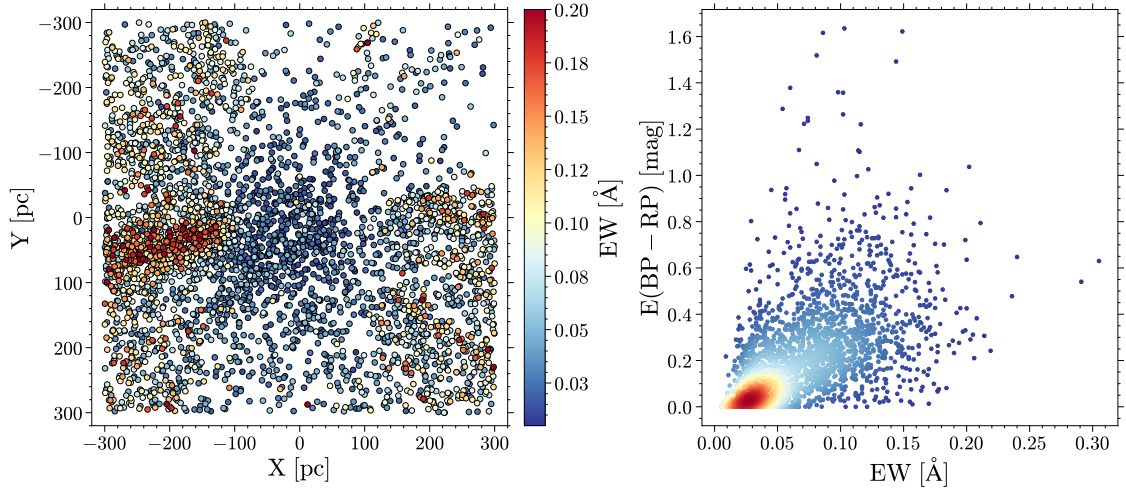


Fig. 14. The Local Bubble: *Left panel:* face-on view of the EW_{862} distribution of 3861 stars with $|X| \leq 300$ pc, $|Y| \leq 300$ pc, and $|Z| \leq 100$ pc. The Galactic centre is located at $(X, Y) = (-8, 0)$. *Right panel:* density plot of the correlation between EW_{862} and $E(BP - RP)$ for 2746 cases with valid $E(BP - RP)$ measurements.

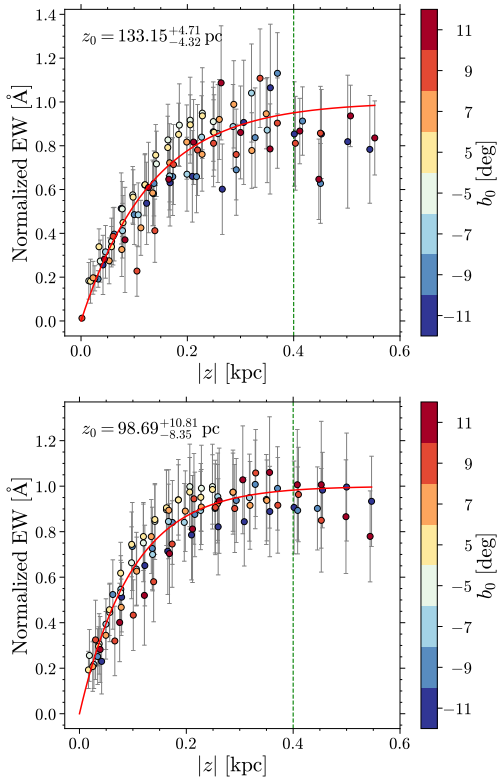


Fig. 15. Determination of the scale height of the $\lambda 862$ carrier by the DIB measurements with $4^\circ \leq |b| \leq 12^\circ$, and *upper panel:* $240^\circ \leq \ell \leq 330^\circ$; *lower panel:* toward all available longitude directions, respectively. The data points at different latitude slabs are coloured according to the central latitude values (b_0). The dashed green line indicates $z = 0.4$ kpc. The red curve in the upper panel is the fit to data points with $z \leq 0.4$ kpc, while in the lower panel, the red curve is the fit to all the data points.

8. Kinematics of the DIB carrier

Although most of the DIB carriers are unknown, they have been proven to be a powerful tool for ISM tomography and consequently can probe the Galactic structure and interstellar environments. The most comprehensive kinematic study to date was performed by Zasowski (2015) using APOGEE (SDSS-III) data, and

allowed the authors to reveal the average Galactic rotation curve of the $\lambda 1527$ DIB carriers spanning several kiloparsecs (kpc) from the Sun. They probed the DIB $\lambda 1527$ carrier distribution in 3D and showed that DIBs $\lambda 1527$ can be used to trace large-scale Galactic structures, such as the Galactic long bar and the warp of the outer disk. Zhao et al. (2021b) studied the kinematics of the DIB $\lambda 862$ in the Galactic Bulge using *Gaia*-ESO (Gilmore et al. 2012) and GIBS data (Zoccali et al. 2014). These authors concluded that the DIB $\lambda 862$ carrier is located in the inner few kpc of the Galactic disk based on their rotation velocities and radial velocity dispersion. However, these studies are based on specific pencil beams with a limited number of objects. Figure 17 demonstrates the enormous potential of *Gaia* for studying the kinematic behaviour of the DIBs $\lambda 862$; it shows the Galactic rotation curve of the DIB $\lambda 862$ carrier for $|b| < 5^\circ$ and in bins of 10 degrees in galactic longitude. Indicated are Galactic rotation curves computed by Model A5 in Reid et al. (2019) with different galactocentric radii (R_{GC}). For sightlines with $\ell \geq 150^\circ$, the DIB $\lambda 862$ velocities are consistent with the model rotation curves for $R_{GC} \sim 9$ kpc. On the other hand, for the inner disc with $\ell \lesssim 30^\circ$ the DIB $\lambda 862$ carrier is best represented by $R_{GC} \sim 7.5$ kpc, thus closer to the Sun. This is different from the findings of Zasowski et al. (2015), namely that the DIB $\lambda 1527$ carrier in the inner Galaxy is farther from the Sun. Indeed, the inner disc sample of these latter authors shows higher velocities compared to our sample by a factor of almost two. This is most likely due to the fact that APOGEE observes in the infrared and so probes the DIB $\lambda 1527$ in the inner Galaxy up to larger distances compared to *Gaia*. The majority of stars in APOGEE are within ~ 6 kpc from the Sun while our sample is mostly confined to $\sim 2\text{--}3$ kpc.

Assuming a galactic rotation model, Zhao et al. (2021b) demonstrated that kinematic distances of the DIB $\lambda 862$ can be obtained, allowing the real 3D distribution of the DIB carrier to be traced. We plan to present this in a forthcoming paper.

Correlations between the DIB $\lambda 862$ carrier and gas kinematics using different tracers such as CO and HI can provide additional clues as to the origin of the DIB $\lambda 862$ carrier. Figure 17 shows one example with the comparison of the ^{12}CO data from Dame et al. (2001). In the present study we use the momentum-masked cube restricted to the latitude range $\pm 5^\circ$. We see that,

¹ <https://lweb.cfa.harvard.edu/rtdc/CO/CompositeSurveys/>

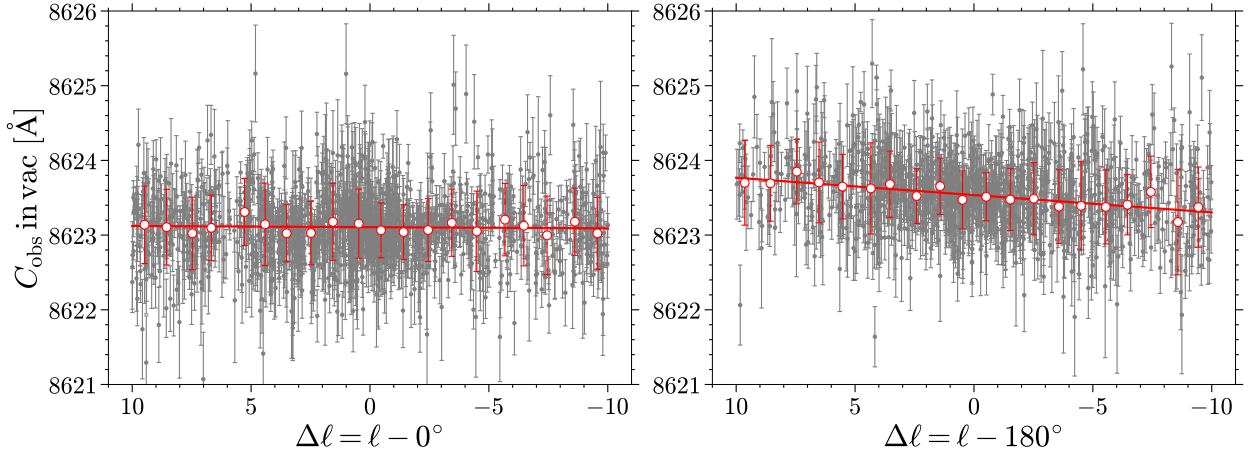


Fig. 16. Observed central wavelengths (C_{obs} , in vacuum) of DIB $\lambda 862$ in the heliocentric frame as a function of the angular distance from the longitude centre ($\Delta\ell$) for the Galactic centre (*left panel*) and the Galactic anti-centre (*right panel*), respectively. The grey points are the individual measurements with the fitted uncertainties. The red dots are the median values taken in each $\Delta\ell = 1^\circ$ bin with the standard deviation. The red lines are the linear fit to the red dots.

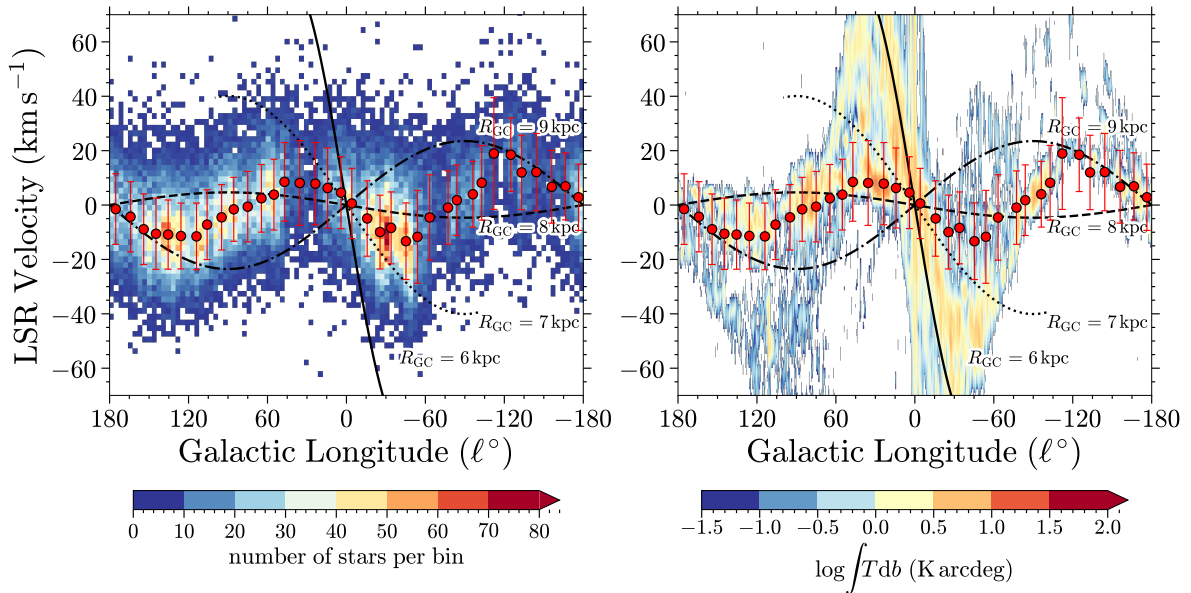


Fig. 17. *Left panel:* longitude–velocity diagram for the *Gaia* HQ DIB $\lambda 862$ sample. The circles indicate the median V_{LSR} and standard uncertainty of the mean for each field. Velocity curves calculated by Model A5 in Reid et al. (2019) for different galactocentric distances (R_{GC}) are overplotted. *Right panel:* same as left panel but superimposed on the ^{12}CO data from Dame et al. (2001). The colour-scale displays the ^{12}CO brightness temperature in a logarithmic scale integrated over the velocity range.

in general, the DIB $\lambda 862$ closely follows the CO gas pattern, especially in the Galactic anticentre region, while higher velocities are seen in CO for $|\ell| < 50^\circ$. This close relation between the DIB $\lambda 862$ and the gas reinforces the suggestion that the DIB $\lambda 862$ carrier could be related to macro molecules. We want to stress again that *Gaia* data allow us to discuss such a large-scale picture for the first time.

9. Conclusions

We present the largest sample of individual DIBs at 862 nm published to date, as obtained by the *Gaia* RVS spectrometer. This is the first homogeneous and all-sky survey of the DIB $\lambda 862$, and allows us to study the global properties of this DIB $\lambda 862$ carrier in detail. Defining a high-quality sample, we demonstrate that DIBs at 862 nm show a tight relation with interstellar reddening

such as $E(\text{BP} - \text{RP})$ or $E(B - V)$. Despite the use of different algorithms in the measurement of DIBs at 862 nm between hot stars ($T_{\text{eff}} > 7000 \text{ K}$) and cool stars ($T_{\text{eff}} \leq 7000 \text{ K}$), we see very similar relations between EW_{862} and $E(\text{BP} - \text{RP})$, demonstrating the robustness of the DIB $\lambda 862$ measurement. While we see similarities in the spatial distributions between the DIB $\lambda 862$ carrier and the interstellar reddening, we also notice some differences, in particular that the scale height of the DIB $\lambda 862$ carrier is smaller compared to the dust and that the DIB $\lambda 862$ carrier is concentrated within the inner kpc from the Sun. A similar conclusion can be drawn from the comparison with the total Galactic extinction map. The main and most striking difference between the DIB $\lambda 862$ carrier and dust distributions is that DIB $\lambda 862$ carriers are present in the Local Bubble around the Sun, while this region is known to contain almost no dust. To first order, the spatial distribution of DIB $\lambda 862$ carriers follows a simple slab

model. We derive its local density and scale height, which can be used to predict the expected EW of the DIB $\lambda 862$ towards any star up to ~ 3 kpc from the Sun.

Taking advantage of the full sky coverage of the DIB $\lambda 862$, we determined the rest-frame wavelength of the DIB $\lambda 862$ in the Galactic anticentre with an estimated $\lambda_0 = 8620.86 \pm 0.019 \text{ \AA}$ in air. This is the most precise determination of λ_0 to date. We note that using a large number of sources diminishes the formal measurement errors and, more importantly, largely negates the systematic errors of unknown radial velocities of clouds of DIB carriers which may influence any studies based on a small number of sources. For the first time, we demonstrate here the Galactic rotation curve traced by the DIB $\lambda 862$ carrier within 1–2 kpc from the Sun and reveal the remarkable correspondence between the DIB $\lambda 862$ velocities and the CO gas velocities, reinforcing the suggestion that DIB $\lambda 862$ carriers could be related to gaseous macromolecules.

Acknowledgements. This work presents results from the European Space Agency (ESA) space mission *Gaia*. *Gaia* data are being processed by the *Gaia* Data Processing and Analysis Consortium (DPAC). Funding for the DPAC is provided by national institutions, in particular the institutions participating in the *Gaia* MultiLateral Agreement (MLA). The *Gaia* mission website is <https://www.cosmos.esa.int/gaia>. The *Gaia* archive website is <https://archives.esac.esa.int/gaia>. Full acknowledgements are given in Appendix A. T.Z. acknowledges financial support of the Slovenian Research Agency (research core funding No. P1-0188) and the European Space Agency (Prodex Experiment Arrangement No. C4000127986). Part of the calculations have been performed with the high-performance computing facility SIGAMM, hosted by the Observatoire de la Côte d’Azur. The GSP-spec group acknowledges financial supports from the french space agency (CNES), Agence Nationale de la Recherche (ANR 14-CE33-014-01) and Programmes Nationaux de Physique Stellaire & Cosmologie et Galaxies (PNPS & PNCG) of CNRS/INSU. H.Z. is funded by the China Scholarship Council (No.201806040200). Y.F. acknowledges the BELgian federal Science Policy Office (BELSPO) through various PROGRAMME de Développement d’Expériences scientifiques (PRODEX) grants.

References

- Adamson, A. J., Whittet, D. C. B., & Duley, W. W. 1991, *MNRAS*, **252**, 234
- Adamson, A. J., Kerr, T. H., Whittet, D. C. B., & Duley, W. W. 1994, *MNRAS*, **268**, 705
- Andrae, R., Fouesneau, M., Sordo, R., et al. 2023, *A&A*, **674**, A27 (*Gaia* DR3 SI)
- Astropy Collaboration (Price-Whelan, A. M., et al.) 2018, *AJ*, **156**, 123
- Bailer-Jones, C. A. L., Rybizki, J., Fouesneau, M., Demleitner, M., & Andrae, R. 2021, *AJ*, **161**, 147
- Bailey, M., van Loon, J. T., Farhang, A., et al. 2016, *A&A*, **585**, A12
- Bovy, J., Allende Prieto, C., Beers, T. C., et al. 2012, *ApJ*, **759**, 131
- Brand, J., & Blitz, L. 1993, *A&A*, **275**, 67
- Brunthaler, A., Menten, K. M., Dzib, S. A., et al. 2021, *A&A*, **651**, A85
- Cami, J., Sonnentrucker, P., Ehrenfreund, P., & Foing, B. H. 1997, *A&A*, **326**, 822
- Capitania, L., Lallement, R., Vergely, J. L., Elyajouri, M., & Monreal-Ibero, A. 2017, *A&A*, **606**, A65
- Chen, H. C., Lallement, R., Babusiaux, C., et al. 2013, *A&A*, **550**, A62
- Churchwell, E., Babler, B. L., Meade, M. R., et al. 2009, *PASP*, **121**, 213
- Clemens, D. P. 1985, *ApJ*, **295**, 422
- Cropper, M., Katz, D., Sartoretti, P., et al. 2018, *A&A*, **616**, A5
- Dame, T. M., Hartmann, D., & Thaddeus, P. 2001, *ApJ*, **547**, 792
- Damineli, A., Almeida, L. A., Blum, R. D., et al. 2016, *MNRAS*, **463**, 2653
- Delchambre, L., Bailer-Jones, C. A. L., Bellas-Velidis, I., et al. 2023, *A&A*, **674**, A31 (*Gaia* DR3 SI)
- Drimmel, R., & Spergel, D. N. 2001, *ApJ*, **556**, 181
- Elyajouri, M., & Lallement, R. 2019, *A&A*, **628**, A67
- Fan, H., Hobbs, L. M., Dahlstrom, J. A., et al. 2019, *ApJ*, **878**, 151
- Farhang, A., van Loon, J. T., Khosroshahi, H. G., Javadi, A., & Bailey, M. 2019, *Nat. Astron.*, **3**, 922
- Gaia Collaboration 2022, *Gaia* DR3 online documentation, <https://gea.esac.esa.int/archive/documentation/GDR3/>
- Galazutdinov, G. A., Krelowski, J., Musaev, F. A., Ehrenfreund, P., & Foing, B. H. 2000a, *MNRAS*, **317**, 750
- Galazutdinov, G. A., Musaev, F. A., Krelowski, J., & Walker, G. A. H. 2000b, *PASP*, **112**, 648
- Galazutdinov, G. A., Lo Curto, G., & Krelowski, J. 2008, *MNRAS*, **386**, 2003
- Geary, J. C. 1975, Ph.D. Thesis, The University of Arizona, USA
- Gershman, S. J., & Blei, D. M. 2012, *J. Math. Psychol.*, **56**, 1
- Gilmore, G., Randich, S., Asplund, M., et al. 2012, *The Messenger*, **147**, 25
- Green, G. M. 2018, *J. Open Source Softw.*, **3**, 695
- Green, G. M., Schlafly, E., Zucker, C., Speagle, J. S., & Finkbeiner, D. 2019, *ApJ*, **887**, 93
- Guo, H. L., Chen, B. Q., Yuan, H. B., et al. 2021, *ApJ*, **906**, 47
- Herbig, G. H. 1995, *ARA&A*, **33**, 19
- Herbig, G. H., & Leka, K. D. 1991, *ApJ*, **382**, 193
- Hunter, J. D. 2007, *Comput. Sci. Eng.*, **9**, 90
- Jenniskens, P., & Desert, F. X. 1994, *A&AS*, **106**, 39
- Jones, D. O., West, A. A., & Foster, J. B. 2011, *AJ*, **142**, 44
- Kerr, T. H., Hibbins, R. E., Fossey, S. J., Miles, J. R., & Sarre, P. J. 1998, *ApJ*, **495**, 941
- Kos, J. 2017, *MNRAS*, **468**, 4255
- Kos, J., Zwitter, T., Grebel, E. K., et al. 2013, *ApJ*, **778**, 86
- Kos, J., Zwitter, T., Wyse, R., et al. 2014, *Science*, **345**, 791
- Krelowski, J. 2018, *PASP*, **130**, 071001
- Krelowski, J., Galazutdinov, G., Godunova, V., & Bondar, A. 2019, *Acta Astron.*, **69**, 159
- Lallement, R., Vergely, J. L., Valette, B., et al. 2014, *A&A*, **561**, A91
- Lallement, R., Babusiaux, C., Vergely, J. L., et al. 2019, *A&A*, **625**, A135
- Lan, T.-W., Ménard, B., & Zhu, G. 2015, *MNRAS*, **452**, 3629
- Leger, A., & Puget, J. L. 1984, *A&A*, **500**, 279
- Li, L., Shen, S., Hou, J., et al. 2018, *ApJ*, **858**, 75
- Maíz Apellániz, J. 2015, *Mem. Soc. Astron. It.*, **86**, 553
- Marshall, D. J., Robin, A. C., Reylé, C., Schultheis, M., & Picaud, S. 2006, *A&A*, **453**, 635
- Merrill, P. W. 1930, *ApJ*, **72**, 98
- Munari, U. 1999, *Balt. Astron.*, **8**, 73
- Munari, U. 2000, *Italian Physical Society Conf. Proc.*, **67**, 179
- Munari, U., Tomasella, L., Fiorucci, M., et al. 2008, *A&A*, **488**, 969
- Ochsenbein, F., Bauer, P., & Marcout, J. 2000, *A&AS*, **143**, 23
- Pérez, F., & Granger, B. E. 2007, *Comput. Sci. Eng.*, **9**, 21
- Planck Collaboration Int. XLVIII 2016, *A&A*, **596**, A109
- Poggio, E., Drimmel, R., Cantat-Gaudin, T., et al. 2021, *A&A*, **651**, A104
- Puget, J. L., & Leger, A. 1989, *ARA&A*, **27**, 161
- Puspitarini, L., Lallement, R., Babusiaux, C., et al. 2015, *A&A*, **573**, A35
- Recio-Blanco, A., de Laverny, P., Palicio, P. A. 2023, *A&A*, **674**, A29 (*Gaia* DR3 SI)
- Reid, M. J., Menten, K. M., Brunthaler, A., et al. 2019, *ApJ*, **885**, 131
- Rezaei Kh, S., Bailer-Jones, C. A. L., Hogg, D. W., & Schultheis, M. 2018, *A&A*, **618**, A168
- Rezaei Kh, S., Bailer-Jones, C. A. L., Soler, J. D., & Zari, E. 2020, *A&A*, **643**, A151
- Sanders, D. B., Solomon, P. M., & Scoville, N. Z. 1984, *ApJ*, **276**, 182
- Sanner, F., Snell, R., & vanden Bout, P. 1978, *ApJ*, **226**, 460
- Sarre, P. J. 2006, *J. Mol. Spectrosc.*, **238**, 1
- Sarre, P. J., Miles, J. R., Kerr, T. H., et al. 1995, *MNRAS*, **277**, L41
- Sartoretti, P., Katz, D., Cropper, M., et al. 2018, *A&A*, **616**, A6
- Schlafly, E. F., & Finkbeiner, D. P. 2011, *ApJ*, **737**, 103
- Schlegel, D. J., Finkbeiner, D. P., & Davis, M. 1998, *ApJ*, **500**, 525
- Snow, T. P., & McCall, B. J. 2006, *ARA&A*, **44**, 367
- Steinmetz, M., Zwitter, T., Siebert, A., et al. 2006, *AJ*, **132**, 1645
- Steinmetz, M., Guiglion, G., McMillan, P. J., et al. 2020, *AJ*, **160**, 83
- Taylor, M. B. 2005, *ASP Conf. Ser.*, **347**, 29
- Vergely, J. L., Freire Ferrero, R., Siebert, A., & Valette, B. 2001, *A&A*, **366**, 1016
- Vergely, J. L., Valette, B., Lallement, R., & Raimond, S. 2010, *A&A*, **518**, A31
- Vos, D. A. I., Cox, N. L. J., Kaper, L., Spaans, M., & Ehrenfreund, P. 2011, *A&A*, **533**, A129
- Wallerstein, G., Sandstrom, K., & Gredel, R. 2007, *PASP*, **119**, 1268
- Welsh, B. Y., Lallement, R., Vergely, J. L., & Raimond, S. 2010, *A&A*, **510**, A54
- Wenger, M., Ochsenbein, F., Egret, D., et al. 2000, *A&AS*, **143**, 9
- Zasowski, G. 2015, *Mem. Soc. Astron. It.*, **86**, 521
- Zasowski, G., Ménard, B., Bizyaev, D., et al. 2015, *ApJ*, **798**, 35
- Zhao, H., Schultheis, M., Recio-Blanco, A., et al. 2021a, *A&A*, **645**, A14
- Zhao, H., Schultheis, M., Rojas-Arriagada, A., et al. 2021b, *A&A*, **654**, A116
- Zoccali, M., Gonzalez, O. A., Vasquez, S., et al. 2014, *A&A*, **562**, A66
- Zucker, C., Speagle, J. S., Schlafly, E. F., et al. 2020, *A&A*, **633**, A51

- 1 Université Côte d'Azur, Observatoire de la Côte d'Azur, CNRS, Laboratoire Lagrange, Bd de l'Observatoire, CS 34229, 06304 Nice Cedex 4, France
- 2 Faculty of Mathematics and Physics, University of Ljubljana, Jadranska ulica 19, 1000 Ljubljana, Slovenia
- 3 IRAP, Université de Toulouse, CNRS, UPS, CNES, 9 Av. Colonel Roche, BP 44346, 31028 Toulouse Cedex 4, France
- 4 INAF – Osservatorio Astrofisico di Torino, via Osservatorio 20, 10025 Pino Torinese (TO), Italy
- 5 Royal Observatory of Belgium, Ringlaan 3, 1180 Brussels, Belgium
- 6 Max Planck Institute for Astronomy, Königstuhl 17, 69117 Heidelberg, Germany
- 7 INAF – Osservatorio astronomico di Padova, Vicolo Osservatorio 5, 35122 Padova, Italy
- 8 Leiden Observatory, Leiden University, Niels Bohrweg 2, 2333 CA Leiden, The Netherlands
- 9 European Space Agency (ESA), European Space Research and Technology Centre (ESTEC), Keplerlaan 1, 2201AZ Noordwijk, The Netherlands
- 10 GEPI, Observatoire de Paris, Université PSL, CNRS, 5 Place Jules Janssen, 92190 Meudon, France
- 11 Univ. Grenoble Alpes, CNRS, IPAG, 38000 Grenoble, France
- 12 Astronomisches Rechen-Institut, Zentrum für Astronomie der Universität Heidelberg, Mönchhofstr. 12-14, 69120 Heidelberg, Germany
- 13 Laboratoire d'astrophysique de Bordeaux, Univ. Bordeaux, CNRS, B18N, allée Geoffroy Saint-Hilaire, 33615 Pessac, France
- 14 Institute of Astronomy, University of Cambridge, Madingley Road, Cambridge CB3 0HA, UK
- 15 Department of Astronomy, University of Geneva, Chemin Pegasi 51, 1290 Versoix, Switzerland
- 16 European Space Agency (ESA), European Space Astronomy Centre (ESAC), Camino bajo del Castillo, s/n, Urbanizacion Villafranca del Castillo, Villanueva de la Cañada, 28692 Madrid, Spain
- 17 Aurora Technology for European Space Agency (ESA), Camino bajo del Castillo, s/n, Urbanizacion Villafranca del Castillo, Villanueva de la Cañada, 28692 Madrid, Spain
- 18 Institut de Ciències del Cosmos (ICCUB), Universitat de Barcelona (IEEC-UB), Martí i Franquès 1, 08028 Barcelona, Spain
- 19 Lohrmann Observatory, Technische Universität Dresden, Mommsenstraße 13, 01062 Dresden, Germany
- 20 Lund Observatory, Department of Astronomy and Theoretical Physics, Lund University, Box 43, 22100 Lund, Sweden
- 21 CNES Centre Spatial de Toulouse, 18 avenue Edouard Belin, 31401 Toulouse Cedex 9, France
- 22 Institut d'Astronomie et d'Astrophysique, Université Libre de Bruxelles CP 226, Boulevard du Triomphe, 1050 Brussels, Belgium
- 23 F.R.S.-FNRS, Rue d'Egmont 5, 1000 Brussels, Belgium
- 24 INAF – Osservatorio Astrofisico di Arcetri, Largo Enrico Fermi 5, 50125 Firenze, Italy
- 25 European Space Agency (ESA), Noordwijk, The Netherlands
- 26 University of Turin, Department of Physics, Via Pietro Giuria 1, 10125 Torino, Italy
- 27 INAF – Osservatorio di Astrofisica e Scienza dello Spazio di Bologna, via Piero Gobetti 93/3, 40129 Bologna, Italy
- 28 DAPCOM for Institut de Ciències del Cosmos (ICCUB), Universitat de Barcelona (IEEC-UB), Martí i Franquès 1, 08028 Barcelona, Spain
- 29 Observational Astrophysics, Division of Astronomy and Space Physics, Department of Physics and Astronomy, Uppsala University, Box 516, 751 20 Uppsala, Sweden
- 30 ALTEC S.p.a, Corso Marche, 79, 10146 Torino, Italy
- 31 Sednai Sàrl, Geneva, Switzerland
- 32 Department of Astronomy, University of Geneva, Chemin d'Ecogia 16, 1290 Versoix, Switzerland
- 33 Mullard Space Science Laboratory, University College London, Holmbury St Mary, Dorking, Surrey RH5 6NT, UK
- 34 Gaia DPAC Project Office, ESAC, Camino bajo del Castillo, s/n, Urbanizacion Villafranca del Castillo, Villanueva de la Cañada, 28692 Madrid, Spain
- 35 Telespazio UK S.L. for European Space Agency (ESA), Camino bajo del Castillo, s/n, Urbanizacion Villafranca del Castillo, Villanueva de la Cañada, 28692 Madrid, Spain
- 36 SYRTE, Observatoire de Paris, Université PSL, CNRS, Sorbonne Université, LNE, 61 avenue de l'Observatoire, 75014 Paris, France
- 37 National Observatory of Athens, I. Metaxa and Vas. Pavlou, Palaia Penteli, 15236 Athens, Greece
- 38 IMCCE, Observatoire de Paris, Université PSL, CNRS, Sorbonne Université, Univ. Lille, 77 av. Denfert-Rochereau, 75014 Paris, France
- 39 Serco Gestión de Negocios for European Space Agency (ESA), Camino bajo del Castillo, s/n, Urbanizacion Villafranca del Castillo, Villanueva de la Cañada, 28692 Madrid, Spain
- 40 Institut d'Astrophysique et de Géophysique, Université de Liège, 19c, Allée du 6 Août, 4000 Liège, Belgium
- 41 CRAAG – Centre de Recherche en Astronomie, Astrophysique et Géophysique, Route de l'Observatoire Bp 63 Bouzareah, 16340 Alger, Algeria
- 42 Institute for Astronomy, University of Edinburgh, Royal Observatory, Blackford Hill, Edinburgh EH9 3HJ, UK
- 43 RHEA for European Space Agency (ESA), Camino bajo del Castillo, s/n, Urbanizacion Villafranca del Castillo, Villanueva de la Cañada, 28692 Madrid, Spain
- 44 ATG Europe for European Space Agency (ESA), Camino bajo del Castillo, s/n, Urbanizacion Villafranca del Castillo, Villanueva de la Cañada, 28692 Madrid, Spain
- 45 CIGUS CITIC – Department of Computer Science and Information Technologies, University of A Coruña, Campus de Elviña s/n, A Coruña 15071, Spain
- 46 Université de Strasbourg, CNRS, Observatoire astronomique de Strasbourg, UMR 7550, 11 rue de l'Université, 67000 Strasbourg, France
- 47 Kavli Institute for Cosmology Cambridge, Institute of Astronomy, Madingley Road, Cambridge CB3 0HA, UK
- 48 Leibniz Institute for Astrophysics Potsdam (AIP), An der Sternwarte 16, 14482 Potsdam, Germany
- 49 CENTRA, Faculdade de Ciências, Universidade de Lisboa, Edif. C8, Campo Grande, 1749-016 Lisboa, Portugal
- 50 Department of Informatics, Donald Bren School of Information and Computer Sciences, University of California, Irvine, 5226 Donald Bren Hall, 92697-3440, CA Irvine, USA
- 51 INAF – Osservatorio Astrofisico di Catania, via S. Sofia 78, 95123 Catania, Italy
- 52 Dipartimento di Fisica e Astronomia "Ettore Majorana", Università di Catania, Via S. Sofia 64, 95123 Catania, Italy
- 53 INAF – Osservatorio Astronomico di Roma, Via Frascati 33, 00078 Monte Porzio Catone (Roma), Italy
- 54 Space Science Data Center – ASI, Via del Politecnico SNC, 00133 Roma, Italy
- 55 Department of Physics, University of Helsinki, PO Box 64, 00014 Helsinki, Finland
- 56 Finnish Geospatial Research Institute FGI, Geodeetinrinne 2, 02430 Masala, Finland
- 57 Institut UTINAM CNRS UMR6213, Université Bourgogne Franche-Comté, OSU THETA Franche-Comté Bourgogne, Observatoire de Besançon, BP1615, 25010 Besançon Cedex, France
- 58 HE Space Operations BV for European Space Agency (ESA), Keplerlaan 1, 2201 AZ Noordwijk, The Netherlands
- 59 Dpto. de Inteligencia Artificial, UNED, c/ Juan del Rosal 16, 28040 Madrid, Spain
- 60 Konkoly Observatory, Research Centre for Astronomy and Earth Sciences, Eötvös Loránd Research Network (ELKH), MTA Centre of Excellence, Konkoly Thege Miklós út 15-17, 1121 Budapest, Hungary

- ⁶¹ ELTE Eötvös Loránd University, Institute of Physics, 1117, Pázmány Péter sétány 1A, Budapest, Hungary
- ⁶² Instituut voor Sterrenkunde, KU Leuven, Celestijnenlaan 200D, 3001 Leuven, Belgium
- ⁶³ Department of Astrophysics/IMAPP, Radboud University, PO Box 9010, 6500 GL Nijmegen, The Netherlands
- ⁶⁴ University of Vienna, Department of Astrophysics, Türkenschanzstraße 17, A1180 Vienna, Austria
- ⁶⁵ Institute of Physics, Laboratory of Astrophysics, Ecole Polytechnique Fédérale de Lausanne (EPFL), Observatoire de Sauverny, 1290 Versoix, Switzerland
- ⁶⁶ Kapteyn Astronomical Institute, University of Groningen, Landleven 12, 9747 AD Groningen, The Netherlands
- ⁶⁷ School of Physics and Astronomy/Space Park Leicester, University of Leicester, University Road, Leicester LE1 7RH, UK
- ⁶⁸ Thales Services for CNES Centre Spatial de Toulouse, 18 avenue Edouard Belin, 31401 Toulouse Cedex 9, France
- ⁶⁹ Depto. Estadística e Investigación Operativa. Universidad de Cádiz, Avda. República Saharaui s/n, 11510 Puerto Real, Cádiz, Spain
- ⁷⁰ Center for Research and Exploration in Space Science and Technology, University of Maryland Baltimore County, 1000 Hilltop Circle, Baltimore, MD, USA
- ⁷¹ GSFC – Goddard Space Flight Center, Code 698, 8800 Greenbelt Rd, 20771, MD Greenbelt, USA
- ⁷² EURIX S.r.l., Corso Vittorio Emanuele II 61, 10128 Torino, Italy
- ⁷³ Porter School of the Environment and Earth Sciences, Tel Aviv University, Tel Aviv 6997801, Israel
- ⁷⁴ Harvard-Smithsonian Center for Astrophysics, 60 Garden St., MS 15, Cambridge, MA 02138, USA
- ⁷⁵ HE Space Operations BV for European Space Agency (ESA), Camino bajo del Castillo, s/n, Urbanizacion Villafranca del Castillo, Villanueva de la Cañada, 28692 Madrid, Spain
- ⁷⁶ Instituto de Astrofísica e Ciências do Espaço, Universidade do Porto, CAUP, Rua das Estrelas, 4150-762 Porto, Portugal
- ⁷⁷ LFCA/DAS, Universidad de Chile, CNRS, Casilla 36-D, Santiago, Chile
- ⁷⁸ SISSA – Scuola Internazionale Superiore di Studi Avanzati, via Bonomea 265, 34136 Trieste, Italy
- ⁷⁹ Telespazio for CNES Centre Spatial de Toulouse, 18 avenue Edouard Belin, 31401 Toulouse Cedex 9, France
- ⁸⁰ University of Turin, Department of Computer Sciences, Corso Svizzera 185, 10149 Torino, Italy
- ⁸¹ Dpto. de Matemática Aplicada y Ciencias de la Computación, Univ. de Cantabria, ETS Ingenieros de Caminos, Canales y Puertos, Avda. de los Castros s/n, 39005 Santander, Spain
- ⁸² Centro de Astronomía – CITEVA, Universidad de Antofagasta, Avenida Angamos 601, Antofagasta 1270300, Chile
- ⁸³ DLR Gesellschaft für Raumfahrtanwendungen (GfR) mbH, Münchener Straße 20, 82234 Weßling, Germany
- ⁸⁴ Centre for Astrophysics Research, University of Hertfordshire, College Lane, AL10 9AB Hatfield, UK
- ⁸⁵ University of Turin, Mathematical Department “G.Peano”, Via Carlo Alberto 10, 10123 Torino, Italy
- ⁸⁶ INAF – Osservatorio Astronomico d’Abruzzo, Via Mentore Maggini, 64100 Teramo, Italy
- ⁸⁷ Instituto de Astronomia, Geofísica e Ciências Atmosféricas, Universidade de São Paulo, Rua do Matão, 1226, Cidade Universitaria, 05508-900 São Paulo, SP, Brazil
- ⁸⁸ APAVE SUDEUROPE SAS for CNES Centre Spatial de Toulouse, 18 avenue Edouard Belin, 31401 Toulouse Cedex 9, France
- ⁸⁹ Mésocentre de calcul de Franche-Comté, Université de Franche-Comté, 16 route de Gray, 25030 Besançon Cedex, France
- ⁹⁰ ATOS for CNES Centre Spatial de Toulouse, 18 avenue Edouard Belin, 31401 Toulouse Cedex 9, France
- ⁹¹ School of Physics and Astronomy, Tel Aviv University, Tel Aviv 6997801, Israel
- ⁹² Astrophysics Research Centre, School of Mathematics and Physics, Queen’s University Belfast, Belfast BT7 INN, UK
- ⁹³ Centre de Données Astronomique de Strasbourg, Strasbourg, France
- ⁹⁴ Institute for Computational Cosmology, Department of Physics, Durham University, Durham DH1 3LE, UK
- ⁹⁵ European Southern Observatory, Karl-Schwarzschild-Str. 2, 85748 Garching, Germany
- ⁹⁶ Max-Planck-Institut für Astrophysik, Karl-Schwarzschild-Straße 1, 85748 Garching, Germany
- ⁹⁷ Data Science and Big Data Lab, Pablo de Olavide University, 41013 Seville, Spain
- ⁹⁸ Barcelona Supercomputing Center (BSC), Plaça Eusebi Güell 1-3, 08034 Barcelona, Spain
- ⁹⁹ ETSE Telecomunicación, Universidade de Vigo, Campus Lagoas-Marcosende, 36310 Vigo, Galicia, Spain
- ¹⁰⁰ Asteroid Engineering Laboratory, Space Systems, Luleå University of Technology, Box 848, 981 28 Kiruna, Sweden
- ¹⁰¹ Vera C Rubin Observatory, 950 N. Cherry Avenue, Tucson, AZ 85719, USA
- ¹⁰² Department of Astrophysics, Astronomy and Mechanics, National and Kapodistrian University of Athens, Panepistimiopolis, Zografos, 15783 Athens, Greece
- ¹⁰³ TRUMPF Photonic Components GmbH, Lise-Meitner-Straße 13, 89081 Ulm, Germany
- ¹⁰⁴ IAC – Instituto de Astrofísica de Canarias, Via Láctea s/n, 38200 La Laguna S.C., Tenerife, Spain
- ¹⁰⁵ Department of Astrophysics, University of La Laguna, Via Láctea s/n, 38200 La Laguna S.C., Tenerife, Spain
- ¹⁰⁶ Faculty of Aerospace Engineering, Delft University of Technology, Kluyverweg 1, 2629 HS Delft, The Netherlands
- ¹⁰⁷ Radagast Solutions, Simon Vestdijkpad 24, 2321WD Leiden, The Netherlands
- ¹⁰⁸ Laboratoire Univers et Particules de Montpellier, CNRS Université Montpellier Place Eugène Bataillon, CC72, 34095 Montpellier Cedex 05, France
- ¹⁰⁹ Université de Caen Normandie, Côte de Nacre Boulevard Maréchal Juin, 14032 Caen, France
- ¹¹⁰ LESIA, Observatoire de Paris, Université PSL, CNRS, Sorbonne Université, Université de Paris, 5 Place Jules Janssen, 92190 Meudon, France
- ¹¹¹ SRON Netherlands Institute for Space Research, Niels Bohrweg 4, 2333 CA Leiden, The Netherlands
- ¹¹² Astronomical Observatory, University of Warsaw, Al. Ujazdowskie 4, 00-478 Warszawa, Poland
- ¹¹³ Scialia for CNES Centre Spatial de Toulouse, 18 avenue Edouard Belin, 31401 Toulouse Cedex 9, France
- ¹¹⁴ Université Rennes, CNRS, IPR (Institut de Physique de Rennes) - UMR 6251, 35000 Rennes, France
- ¹¹⁵ INAF – Osservatorio Astronomico di Capodimonte, Via Moiriello 16, 80131 Napoli, Italy
- ¹¹⁶ Shanghai Astronomical Observatory, Chinese Academy of Sciences, 80 Nandan Road, Shanghai 200030, PR China
- ¹¹⁷ University of Chinese Academy of Sciences, No.19(A) Yuquan Road, Shijingshan District, Beijing 100049, PR China
- ¹¹⁸ Niels Bohr Institute, University of Copenhagen, Juliane Maries Vej 30, 2100 Copenhagen Ø, Denmark
- ¹¹⁹ DXC Technology, Retortvej 8, 2500 Valby, Denmark
- ¹²⁰ Las Cumbres Observatory, 6740 Cortona Drive Suite 102, Goleta, CA 93117, USA
- ¹²¹ CIGUS CITIC, Department of Nautical Sciences and Marine Engineering, University of A Coruña, Paseo de Ronda 51, 15071 A Coruña, Spain
- ¹²² Astrophysics Research Institute, Liverpool John Moores University, 146 Brownlow Hill, Liverpool L3 5RF, UK
- ¹²³ IPAC, Mail Code 100-22, California Institute of Technology, 1200 E. California Blvd., Pasadena, CA 91125, USA
- ¹²⁴ MTA CSFK Lendület Near-Field Cosmology Research Group, Konkoly Observatory, MTA Research Centre for Astronomy and Earth Sciences, Konkoly Thege Miklós út 15-17, 1121 Budapest, Hungary
- ¹²⁵ Departamento de Física de la Tierra y Astrofísica, Universidad Complutense de Madrid, 28040 Madrid, Spain
- ¹²⁶ Ruđer Bošković Institute, Bijenička cesta 54, 10000 Zagreb, Croatia

- ¹²⁷ Villanova University, Department of Astrophysics and Planetary Science, 800 E Lancaster Avenue, Villanova, PA 19085, USA
- ¹²⁸ INAF – Osservatorio Astronomico di Brera, via E. Bianchi, 46, 23807 Merate, (LC), Italy
- ¹²⁹ STFC, Rutherford Appleton Laboratory, Harwell, Didcot OX11 0QX, UK
- ¹³⁰ Charles University, Faculty of Mathematics and Physics, Astronomical Institute of Charles University, V Holesovickach 2, 18000 Prague, Czech Republic
- ¹³¹ Department of Particle Physics and Astrophysics, Weizmann Institute of Science, Rehovot 7610001, Israel
- ¹³² Department of Astrophysical Sciences, 4 Ivy Lane Princeton University, Princeton, NJ 08544, USA
- ¹³³ Departamento de Astrofísica, Centro de Astrobiología (CSIC-INTA), ESA-ESAC, Camino Bajo del Castillo s/n., 28692 Villanueva de la Cañada, Madrid, Spain
- ¹³⁴ naXys, University of Namur, Rempart de la Vierge, 5000 Namur, Belgium
- ¹³⁵ CGI Deutschland B.V. & Co. KG, Mornewegstr. 30, 64293 Darmstadt, Germany
- ¹³⁶ Institute of Global Health, University of Geneva, Geneva, Switzerland,
- ¹³⁷ Astronomical Observatory Institute, Faculty of Physics, Adam Mickiewicz University, Poznań, Poland
- ¹³⁸ H H Wills Physics Laboratory, University of Bristol, Tyndall Avenue, Bristol BS8 1TL, UK
- ¹³⁹ Department of Physics and Astronomy G. Galilei, University of Padova, Vicolo dell’Osservatorio 3, 35122 Padova, Italy
- ¹⁴⁰ CERN, Esplanade des Particules 1, PO Box 1211 Geneva, Switzerland
- ¹⁴¹ Applied Physics Department, Universidade de Vigo, 36310 Vigo, Spain
- ¹⁴² Association of Universities for Research in Astronomy, 1331 Pennsylvania Ave. NW, Washington, D.C. 20004, USA
- ¹⁴³ European Southern Observatory, Alonso de Córdova 3107, Casilla 19, Santiago, Chile
- ¹⁴⁴ Sorbonne Université, CNRS, UMR7095, Institut d’Astrophysique de Paris, 98bis bd. Arago, 75014 Paris, France

Appendix A: Full acknowledgements

The *Gaia* mission and data processing have financially been supported by, in alphabetical order by country:

- the Algerian Centre de Recherche en Astronomie, Astrophysique et Géophysique of Bouzareah Observatory;
- the Austrian Fonds zur Förderung der wissenschaftlichen Forschung (FWF) Hertha Firnberg Programme through grants T359, P20046, and P23737;
- the BELgian federal Science Policy Office (BELSPO) through various PROgramme de Développement d'Expériences scientifiques (PRODEX) grants, the Research Foundation Flanders (Fonds Wetenschappelijk Onderzoek) through grant VS.091.16N, the Fonds de la Recherche Scientifique (FNRS), and the Research Council of Katholieke Universiteit (KU) Leuven through grant C16/18/005 (Pushing AsteRoseismology to the next level with TESS, GaiA, and the Sloan DIgital Sky SurVEy – PARADISE);
- the Brazil-France exchange programmes Fundação de Amparo à Pesquisa do Estado de São Paulo (FAPESP) and Coordenação de Aperfeiçoamento de Pessoal de Nível Superior (CAPES) - Comité Français d'Evaluation de la Coopération Universitaire et Scientifique avec le Brésil (COFECUB);
- the Chilean Agencia Nacional de Investigación y Desarrollo (ANID) through Fondo Nacional de Desarrollo Científico y Tecnológico (FONDECYT) Regular Project 1210992 (L. Chemin);
- the National Natural Science Foundation of China (NSFC) through grants 11573054, 11703065, and 12173069, the China Scholarship Council through grant 201806040200, and the Natural Science Foundation of Shanghai through grant 21ZR1474100;
- the Tenure Track Pilot Programme of the Croatian Science Foundation and the École Polytechnique Fédérale de Lausanne and the project TTP-2018-07-1171 'Mining the Variable Sky', with the funds of the Croatian-Swiss Research Programme;
- the Czech-Republic Ministry of Education, Youth, and Sports through grant LG 15010 and INTER-EXCELLENCE grant LTAUSA18093, and the Czech Space Office through ESA PECS contract 98058;
- the Danish Ministry of Science;
- the Estonian Ministry of Education and Research through grant IUT40-1;
- the European Commission's Sixth Framework Programme through the European Leadership in Space Astrometry (ELSA) Marie Curie Research Training Network (MRTN-CT-2006-033481), through Marie Curie project PIOFGA-2009-255267 (Space AsteroSeismology & RR Lyrae stars, SAS-RRL), and through a Marie Curie Transfer-of-Knowledge (ToK) fellowship (MTKD-CT-2004-014188); the European Commission's Seventh Framework Programme through grant FP7-606740 (FP7-SPACE-2013-1) for the *Gaia* European Network for Improved data User Services (GENIUS) and through grant 264895 for the *Gaia* Research for European Astronomy Training (GREAT-ITN) network;
- the European Cooperation in Science and Technology (COST) through COST Action CA18104 'Revealing the Milky Way with *Gaia* (MW-Gaia)';
- the European Research Council (ERC) through grants 320360, 647208, and 834148 and through the European Union's Horizon 2020 research and innovation and excellent science programmes through Marie Skłodowska-Curie grant 745617 (Our Galaxy at full HD – Gal-HD) and 895174 (The build-up and fate of self-gravitating systems in the Universe) as well as grants 687378 (Small Bodies: Near and Far), 682115 (Using the Magellanic Clouds to Understand the Interaction of Galaxies), 695099 (A sub-percent distance scale from binaries and Cepheids – CepBin), 716155 (Structured ACCREtion Disks – SACCRED), 951549 (Sub-percent calibration of the extragalactic distance scale in the era of big surveys – UniverScale), and 101004214 (Innovative Scientific Data Exploration and Exploitation Applications for Space Sciences – EXPLORE);
- the European Science Foundation (ESF), in the framework of the *Gaia* Research for European Astronomy Training Research Network Programme (GREAT-ESF);
- the European Space Agency (ESA) in the framework of the *Gaia* project, through the Plan for European Cooperating States (PECS) programme through contracts C98090 and 4000106398/12/NL/KML for Hungary, through contract 4000115263/15/NL/IB for Germany, and through PROgramme de Développement d'Expériences scientifiques (PRODEX) grant 4000127986 for Slovenia;
- the Academy of Finland through grants 299543, 307157, 325805, 328654, 336546, and 345115 and the Magnus Ehrnrooth Foundation;
- the French Centre National d'Études Spatiales (CNES), the Agence Nationale de la Recherche (ANR) through grant ANR-10-IDEX-0001-02 for the 'Investissements d'avenir' programme, through grant ANR-15-CE31-0007 for project 'Modelling the Milky Way in the *Gaia* era' (MOD4Gaia), through grant ANR-14-CE33-0014-01 for project 'The Milky Way disc formation in the *Gaia* era' (ARCHEOGAL), through grant ANR-15-CE31-0012-01 for project 'Unlocking the potential of Cepheids as primary distance calibrators' (UnlockCepheids), through grant ANR-19-CE31-0017 for project 'Secular evolution of galaxies' (SEGAL), and through grant ANR-18-CE31-0006 for project 'Galactic Dark Matter' (GaDaMa), the Centre National de la Recherche Scientifique (CNRS) and its SNO *Gaia* of the Institut des Sciences de l'Univers (INSU), its Programmes Nationaux: Cosmologie et Galaxies (PNCG), Gravitation Références Astronomie Métrologie (PNGRAM), Planétologie (PNP), Physique et Chimie du Milieu Interstellaire (PCMI), and Physique Stellaire (PNPS), the 'Action Fédératrice *Gaia*' of the Observatoire de Paris, the Région de Franche-Comté, the Institut National Polytechnique (INP) and the Institut National de Physique nucléaire et de Physique des Particules (IN2P3) co-funded by CNES;
- the German Aerospace Agency (Deutsches Zentrum für Luft- und Raumfahrt e.V., DLR) through grants 50QG0501, 50QG0601, 50QG0602, 50QG0701, 50QG0901, 50QG1001, 50QG1101, 50QG1401, 50QG1402, 50QG1403, 50QG1404, 50QG1904, 50QG2101, 50QG2102, and 50QG2202, and the Centre for Information Services and High Performance Computing (ZIH) at the Technische Universität Dresden for generous allocations of computer time;
- the Hungarian Academy of Sciences through the Lendület Programme grants LP2014-17 and LP2018-7 and the Hungarian National Research, Development, and Innovation Office (NKFIH) through grant KKP-137523 ('SeismoLab');
- the Science Foundation Ireland (SFI) through a Royal Society - SFI University Research Fellowship (M. Fraser);
- the Israel Ministry of Science and Technology through grant 3-18143 and the Tel Aviv University Center for

- Artificial Intelligence and Data Science (TAD) through a grant;
- the Agenzia Spaziale Italiana (ASI) through contracts I/037/08/0, I/058/10/0, 2014-025-R.0, 2014-025-R.1.2015, and 2018-24-HH.0 to the Italian Istituto Nazionale di Astrofisica (INAF), contract 2014-049-R.0/1/2 to INAF for the Space Science Data Centre (SSDC, formerly known as the ASI Science Data Center, ASDC), contracts I/008/10/0, 2013/030/I.0, 2013-030-I.0.1-2015, and 2016-17-I.0 to the Aerospace Logistics Technology Engineering Company (ALTEC S.p.A.), INAF, and the Italian Ministry of Education, University, and Research (Ministero dell’Istruzione, dell’Università e della Ricerca) through the Premiale project ‘Mining The Cosmos Big Data and Innovative Italian Technology for Frontier Astrophysics and Cosmology’ (MITiC);
 - the Netherlands Organisation for Scientific Research (NWO) through grant NWO-M-614.061.414, through a VICI grant (A. Helmi), and through a Spinoza prize (A. Helmi), and the Netherlands Research School for Astronomy (NOVA);
 - the Polish National Science Centre through HARMONIA grant 2018/30/M/ST9/00311 and DAINA grant 2017/27/L/ST9/03221 and the Ministry of Science and Higher Education (MNiSW) through grant DIR/WK/2018/12;
 - the Portuguese Fundação para a Ciência e a Tecnologia (FCT) through national funds, grants SFRH/BD/128840/2017 and PTDC/FIS-AST/30389/2017, and work contract DL 57/2016/CP1364/CT0006, the Fundo Europeu de Desenvolvimento Regional (FEDER) through grant POCI-01-0145-FEDER-030389 and its Programa Operacional Competitividade e Internacionalização (COMPETE2020) through grants UIDB/04434/2020 and UIDP/04434/2020, and the Strategic Programme UIDB/00099/2020 for the Centro de Astrofísica e Gravitação (CENTRA);
 - the Slovenian Research Agency through grant P1-0188;
 - the Spanish Ministry of Economy (MINECO/FEDER, UE), the Spanish Ministry of Science and Innovation (MICIN), the Spanish Ministry of Education, Culture, and Sports, and the Spanish Government through grants BES-2016-078499, BES-2017-083126, BES-C-2017-0085, ESP2016-80079-C2-1-R, ESP2016-80079-C2-2-R, FPU16/03827, PDC2021-121059-C22, RTI2018-095076-B-C22, and TIN2015-65316-P (‘Computación de Altas Prestaciones VII’), the Juan de la Cierva Incorporación Programme (FJCI-2015-2671 and IJC2019-04862-I for F. Anders), the Severo Ochoa Centre of Excellence Programme (SEV2015-0493), and MICIN/AEI/10.13039/501100011033 (and the European Union through European Regional Development Fund ‘A way of making Europe’) through grant RTI2018-095076-B-C21, the Institute of Cosmos Sciences University of Barcelona (ICCUB, Unidad de Excelencia ‘María de Maeztu’) through grant CEX2019-000918-M, the University of Barcelona’s official doctoral programme for the development of an R+D+i project through an Ajuts de Personal Investigador en Formació (APIF) grant, the Spanish Virtual Observatory through project AyA2017-84089, the Galician Regional Government, Xunta de Galicia, through grants ED431B-2021/36, ED481A-2019/155, and ED481A-2021/296, the Centro de Investigación en Tecnologías de la Información y las Comunicaciones (CITIC), funded by the Xunta de Galicia and the European Union (European Regional Development Fund – Galicia 2014-2020 Programme), through grant ED431G-2019/01, the Red Española de Supercomputación (RES) computer resources at MareNostrum, the Barcelona Supercomputing Centre - Centro Nacional de Supercomputación (BSC-CNS) through activities AECT-2017-2-0002, AECT-2017-3-0006, AECT-2018-1-0017, AECT-2018-2-0013, AECT-2018-3-0011, AECT-2019-1-0010, AECT-2019-2-0014, AECT-2019-3-0003, AECT-2020-1-0004, and DATA-2020-1-0010, the Departament d’Innovació, Universitats i Empresa de la Generalitat de Catalunya through grant 2014-SGR-1051 for project ‘Models de Programació i Entorns d’Execució Paralels’ (MPEXPAR), and Ramon y Cajal Fellowship RYC2018-025968-I funded by MICIN/AEI/10.13039/501100011033 and the European Science Foundation (‘Investing in your future’);
 - the Swedish National Space Agency (SNSA/Rymdstyrelsen);
 - the Swiss State Secretariat for Education, Research, and Innovation through the Swiss Activités Nationales Complémentaires and the Swiss National Science Foundation through an Eccellenza Professorial Fellowship (award PCEFP2_194638 for R. Anderson);
 - the United Kingdom Particle Physics and Astronomy Research Council (PPARC), the United Kingdom Science and Technology Facilities Council (STFC), and the United Kingdom Space Agency (UKSA) through the following grants to the University of Bristol, the University of Cambridge, the University of Edinburgh, the University of Leicester, the Mullard Space Sciences Laboratory of University College London, and the United Kingdom Rutherford Appleton Laboratory (RAL): PP/D006511/1, PP/D006546/1, PP/D006570/1, ST/I000852/1, ST/J005045/1, ST/K00056X/1, ST/K000209/1, ST/K000756/1, ST/L006561/1, ST/N000595/1, ST/N000641/1, ST/N000978/1, ST/N001117/1, ST/S000089/1, ST/S000976/1, ST/S000984/1, ST/S001123/1, ST/S001948/1, ST/S001980/1, ST/S002103/1, ST/V000969/1, ST/W002469/1, ST/W002493/1, ST/W002671/1, ST/W002809/1, and EP/V520342/1.
- We made use of the following tools in the preparation of this paper:
- (SIMBAD, [Wenger et al. 2000](#)) and Vizier ([Ochsenbein et al. 2000](#)) operated at (CDS) Strasbourg; NASA ADS; TOPCAT ([Taylor 2005](#)); Matplotlib ([Hunter 2007](#)); IPython ([Pérez & Granger 2007](#)); Astropy, a community-developed core Python package for Astronomy ([Astropy Collaboration 2018](#));
- Funding for SDSS-III has been provided by the Alfred P. Sloan Foundation, the Participating Institutions, the National Science Foundation, and the U.S. Department of Energy Office of Science. The SDSS-III web site is <http://www.sdss3.org/>. SDSS-III is managed by the Astrophysical Research Consortium for the Participating Institutions of the SDSS-III Collaboration including the University of Arizona, the Brazilian Participation Group, Brookhaven National Laboratory, Carnegie Mellon University, University of Florida, the French Participation Group, the German Participation Group, Harvard University, the Instituto de Astrofísica de Canarias, the Michigan State/Notre Dame/JINA Participation Group, Johns Hopkins University, Lawrence Berkeley National Laboratory, Max Planck Institute for Astrophysics, Max Planck Institute for Extraterrestrial Physics, New Mexico State University, New York University, Ohio State University, Pennsylvania State University, University of Portsmouth, Princeton University, the Spanish Participation Group, University of Tokyo, University of Utah, Vanderbilt University, University of Virginia, University of Washington, and Yale University.

Funding for the Sloan Digital Sky Survey IV has been provided by the Alfred P. Sloan Foundation, the U.S. Department of Energy Office of Science, and the Participating Institutions. SDSS-IV acknowledges support and resources from the Center for High Performance Computing at the University of Utah. The SDSS website is www.sdss.org. SDSS-IV is managed by the Astrophysical Research Consortium for the Participating Institutions of the SDSS Collaboration including the Brazilian Participation Group, the Carnegie Institution for Science, Carnegie Mellon University, Center for Astrophysics | Harvard & Smithsonian, the Chilean Participation Group, the French Participation Group, Instituto de Astrofísica de Canarias, The Johns Hopkins University, Kavli Institute for the Physics and Mathematics of the Universe (IPMU) / University of Tokyo, the Korean Participation Group, Lawrence Berkeley National Laboratory, Leibniz Institut für Astrophysik Potsdam (AIP), Max-Planck-Institut für Astronomie (MPIA Heidelberg), Max-Planck-Institut für Astrophysik (MPA Garching), Max-Planck-Institut für Extraterrestrische Physik (MPE), National Astronomical Observatories of China, New Mexico State University, New York University, University of Notre Dame, Observatório Nacional / MCTI, The Ohio State University, Pennsylvania State University, Shanghai Astronomical Observatory, United Kingdom Participation Group, Universidad Nacional Autónoma de México, University of Arizona, University of Colorado Boulder, University of Oxford, University of Portsmouth, University of Utah, University of Virginia, University of Washington, University of Wisconsin, Vanderbilt University, and Yale University.

Appendix B: ADQL Queries

Use Case: Retrieve full DIB sample

```
SELECT *
FROM user_dr3int5.astrophysical_parameters AS
gaia
INNER JOIN user_dr3int5.astrophysical_parameters_
supp AS m
ON gaia.source_id = m.source_id
WHERE gaia.dibqf_gspspec >= 0
```

Use Case: Retrieve DIB results for HQ sample

```
SELECT *
FROM user_dr3int5.astrophysical_parameters
WHERE ((flags_gspspec LIKE '0%') OR (flags_gspspec LIKE
'1%')) AND ((flags_gspspec LIKE '_0%') OR (flags_gspspec
LIKE '_1%')) AND ((flags_gspspec LIKE '__0%') OR
(flags_gspspec LIKE '__1%')) AND ((flags_gspspec
LIKE '___0%') OR (flags_gspspec LIKE '___1%')) AND
((flags_gspspec LIKE '____0%') OR (flags_gspspec LIKE
'____1%')) AND ((flags_gspspec LIKE '_____0%') OR
(flags_gspspec LIKE '_____1%')) AND ((flags_gspspec
LIKE '______0%') OR (flags_gspspec LIKE '______1%'))
AND ((flags_gspspec LIKE '_______0%') OR (flags_gspspec
LIKE '_______1%')) AND ((flags_gspspec LIKE '_______0%')
OR (flags_gspspec LIKE '_______1%')) AND ((flags_gspspec
LIKE '_____0%') OR (flags_gspspec LIKE '_____1%'))
AND ((flags_gspspec LIKE '______0%') OR (flags_gspspec
LIKE '______1%')) AND ((flags_gspspec LIKE '______0%')
OR (flags_gspspec LIKE '______1%')) AND ((flags_gspspec
LIKE '_______0%') OR (flags_gspspec LIKE '_______1%'))
AND ((flags_gspspec LIKE '_______0%') OR (flags_gspspec
LIKE '_______1%')) AND (dibqf_gspspec <= 2) AND
(dibqf_gspspec >= 0 ) AND (dib_gspspec_lambda>
862.0) AND (dib_gspspec_lambda < 862.6) AND
((dibew_gspspec_uncertainty/dibew_gspspec) < 0.35)
```

Appendix C: Hot star outliers

Table C.1. Outliers found in the hot stars sample (Fig. 9). Description of the table columns: number (col.1), GDR3 ID (col.2), Simbad ID and spectral/object type between brackets when available (col.3), effective temperatures from ESP-HS and spectral type found in then field spectraltype_esphs (col.4), GSP-Spec (col.5), and GSP-Phot (col.6).

n	DR3 ID	ID Simbad	Teff ESP-HS	Teff GSP-Spec	Teff GSP-Phot
ESP-HS, upper panel of Fig. 9					
1	2066753415480268800	2MASS J20500395+4300117	54 705 (O)	6 904	7 690
2	444955867385000832	-	54 650 (O)	6 248	7 023
3	4054566946966876288	CD-32 12958	54 706 (B)	7 115	-
4	2164089679515345280	TYC 3589-1199-1	13 541 (B)	8 404	-
5	5537927056196905984	TYC 7659-1313-1	16 054 (B)	8 339	12 109
6	1730824030187372416	FQ Aqr	17 364 (B)	8 289	-
7	3455454953759211264	LS V +35 26 (OB-e)	20 000 (B)	8 068	-
8	2005574977916673792	BD+53 2784 (B3 III)	17 695 (B)	7 869	-
GSP-Phot, middle panel of Fig. 9					
1	5999123049637219072	IRAS 15212-4624	- (M)	7 316	3 641
2	5843278232842959872	IRAS 12365-6959	- (M)	7 312	3 523
3	5878260883212542208	-	- (O)	7 843	6 495
4	5854026787978149760	IRAS 14112-6224	- (M)	8 000	3 712
5	5889006272967734144	IRAS 15230-5132 (LP?)	- (M)	7 348	3 584
6	4152556797623844608	TYC 5702-740-1	- (O)	7 679	8 061
7	4134885451076972416	IRAS 17170-1756	- (M)	7 900	3 707
8	5341747587387330432	IRAS 11464-5753 (M7)	- (M)	7 900	3 500
9	1931994246725494400	V608 And (M7/M8)	- (M)	7 298	3 623
10	4478836843125274496	IRAS 18313+0720	- (M)	8 000	3 637